Prolonged Siberian heat of 2020

Authors
Met Office UK: Andrew Ciavarella, Daniel Cotterill, Peter Stott
KNMI: Sarah Kew, Sjoukje Philip, Geert Jan van Oldenborgh
DWD: Amalie Skålevåg, Philip Lorenz
Météo France: Yoann Robin
University of Oxford: Friederike Otto
ETH Zurich: Mathias Hauser, Sonia I. Seneviratne, Flavio Lehner
IGE/UGA, P.P.Shirshov Institute of Oceanology: Olga Zolina

Published online: https://www.worldweatherattribution.org/siberian-heatwave-of-2020-almost-impossible-without-climate-change
15 July 2020

Table of contents

1 Introduction

Since the beginning of 2020, anomalously high temperatures have repeatedly been reported in Siberia. For instance, on June 17, 2020, the Guardian reported that Russia as a whole had experienced record high temperatures in 2020, with the average from January to May being 5.3°C above the 1951-1980 average[1] and contributing to January to May globally averaged temperatures ranking 2nd warmest on record. On June 23, the World Meteorological Organization (WMO) announced that it was "seeking to verify a reported new record temperature north of the Arctic Circle [of] 38°C on 20 June in the Russian town of Verkhoyansk amid a prolonged Siberian heatwave and increase in wildfire activity"[2]. Subsequently, numerous media (newspapers, televisions, radios) have reported on the event as well as on the Siberian heat anomaly persisting since early 2020. The June 20 Arctic temperature record was then confirmed on June 30 by Russia's meteorological service[3]. It should be noted that this temperature is not reproduced by the (lower than station resolution) ERA5 reanalysis, which only reaches 33.9 ºC on 21 June.

The present report investigates the role of human-induced climate change in the likelihood and intensity of both of these events: a) the persistent warm anomalies across the Siberian region (60–75ºN, 60–180ºE) from January to June 2020 (Figure 1), and b) the reported record temperature of 38°C at Verkhoyansk (67.55ºN, 133.38ºE) on June 20 (Figure 2). Both of these event definitions are chosen primarily to relate to the impacts of the extreme heat.

While the record temperature north of the Arctic circle on June 20 made many headlines, impacts linked directly or in part to the extreme heat have been widespread. Persistent and unusually many wildfires have been observed. About 7,900 square miles of Siberian territory had burned so far this year as of June 25, compared to a total of 6,800 square miles as of the same date a year ago, according to official data, [4][5] these fires led to a release of 56 Megatons of CO2 in June 2020[6], more than the yearly CO2 emissions of some countries (e.g., Switzerland)[7]. High temperatures and also the dry conditions in the first 6 months probably exacerbated these fires. Further impacts include health impacts on the population[8] and the melting of permafrost which led to high damages, including environmental pollution: "A fuel tank near the isolated Arctic mining city of Norilsk burst in late May after sinking into permafrost that had stood firm for years but gave way during a warm spring, officials said. It released about 150,000 barrels of diesel into a river."[9]

It is important to highlight that the meteorological extremes assessed here are only partly representing one component of these described impacts, the hazard, whereas the impacts strongly depend on exposure and vulnerability too, as well as other climatological components of the hazard.

The high temperatures in Siberia in January–April were associated with much lower pressure than normal over the Arctic Ocean, extending south into northern Siberia (Figure 3). In this season low pressure is associated with less cold temperatures as it inhibits the clear skies of the Siberian High that cause strong longwave radiation from the snow. This pattern persisted, being very strong in January–March and less strong in April. It also supports direct advection of relatively warmer and moister from lower latitudes. A detailed analysis of factors that can lead to such situations is provided in Wu and

1 https://www.theguardian.com/environment/2020/jun/17/climate-crisis-alarm-at-record-breaking-heatwave-in-siberia
2 https://public.wmo.int/en/media/news/reported-new-record-temperature-of-38°c-north-of-arctic-circle
3 https://twitter.com/WMO/status/1278995524079824898
4 https://www.nytimes.com/2020/06/25/world/europe/siberia-heat-wave-climate-change.html
5 https://www.nationalgeographic.com/science/2020/07/heat-wave-thawed-siberia-now-on-fire/
6 https://atmosphere.copernicus.eu/another-active-year-arctic-wildfires
7 http://globalcarbonatlas.org/en/CO2-emissions
8 https://www.nytimes.com/2020/06/25/world/europe/siberia-heat-wave-climate-change.html
9 https://www.nytimes.com/2020/06/25/world/europe/siberia-heat-wave-climate-change.html

Chen (2020). In May–June the opposite connection holds: higher pressure gives more sunshine, which increases temperature. We indeed find above-normal sea-level pressure during these months in the study area, although the deviations are small. Persistence of the high temperature anomalies is enhanced during these last months due to earlier snow melt (Figure 4). The bare soil absorbs more solar radiation and hence causes higher temperatures.

The synoptic development that led to the record temperatures in Verkhoyansk (Figure 2) was initially associated with the blocking of the subpolar jet by a persistent low over Central Siberia which happened on 06-08 June 2020 resulting in the formation of a moderately high pressure ridge over eastern Siberia (somewhat east of Verkhoyansk). This pattern likely originated from a cut-off of the North Pacific anticyclone and could be considered to have pre-conditioned the high temperature anomaly in the second part of June. This pattern was characterized by z500 exceeding 558 gpm and MSLP being 1013-1014 at max. Notably daily maximum temperatures increased to 27.8-28.0 °C on 08 June. After 12 June this center started to grow, expanding over much of Eastern Siberia (including Verkhoyansk). Meanwhile the local temperature experienced a short-term decrease during 09-12 June (daily maxima being 10 to 20 ºC) which might be associated with the air-mass transport from the Sea of Okhotsk. Starting from 16-17 June this high pressure center was under the influence of the intense transport of the tropical air masses associated with propagation of the tropical high pressure ridge from the south northeastward. Some earlier studies (e.g. Chol and Ahn 2019) report potential association of such development with the impact of Asian monsoon in spring-early summer time. This resulted in forming a sustained high pressure pattern centered a bit eastward of Verkhoyansk with a maximum z500 located between the Lena and Indigirka rivers exceeding 580 gpm and providing an advection of very hot air from the south. Notably this high pressure system was not as obvious in the surface pressure which revealed moderately high values of 1014-1018 hPa between 18 and 25 June when the maximum surface temperatures reached 36-38 ºC. The local high pressure center started to slightly decay after 27-28 June being shifted westward over Central northern Siberia.

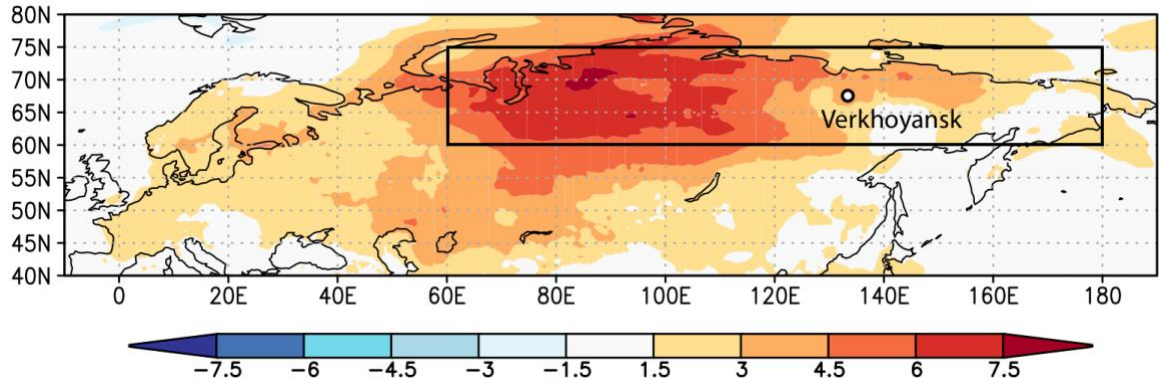

Figure 1: ERA5 near surface temperature (T2m) anomalies [°C] for Jan-Jun 2020. Reference period: 1981-2010. The rectangle represents the study region at 60-75°N, 60-180°E.

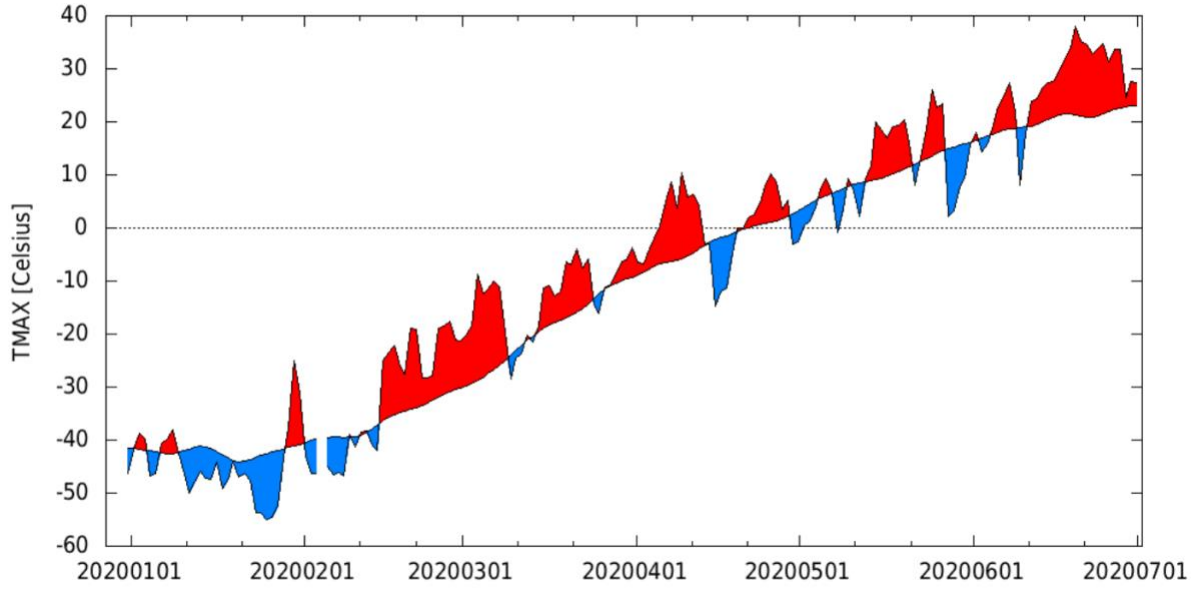

Figure 2: Daily maximum temperature (TX) observations [°C] from January-June 2020 at station Verkhoyansk with positive and negative departures from the 1981-2010 climatological mean shaded red and blue respectively. TX peaks at 38°C on June 20.

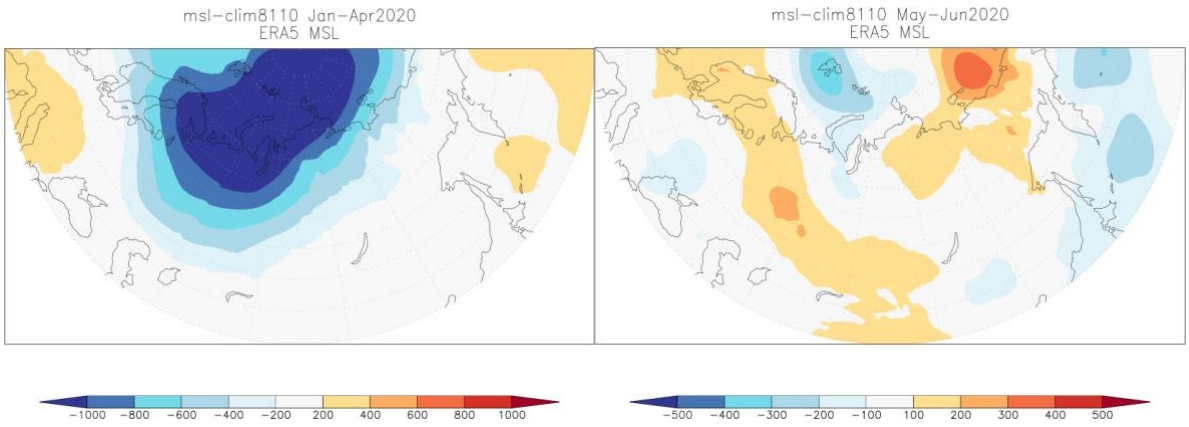

Figure 3: Sea-level pressure anomalies [Pa] in January–April 2020 (left) and May-June 2020 (right). Source: ERA5.

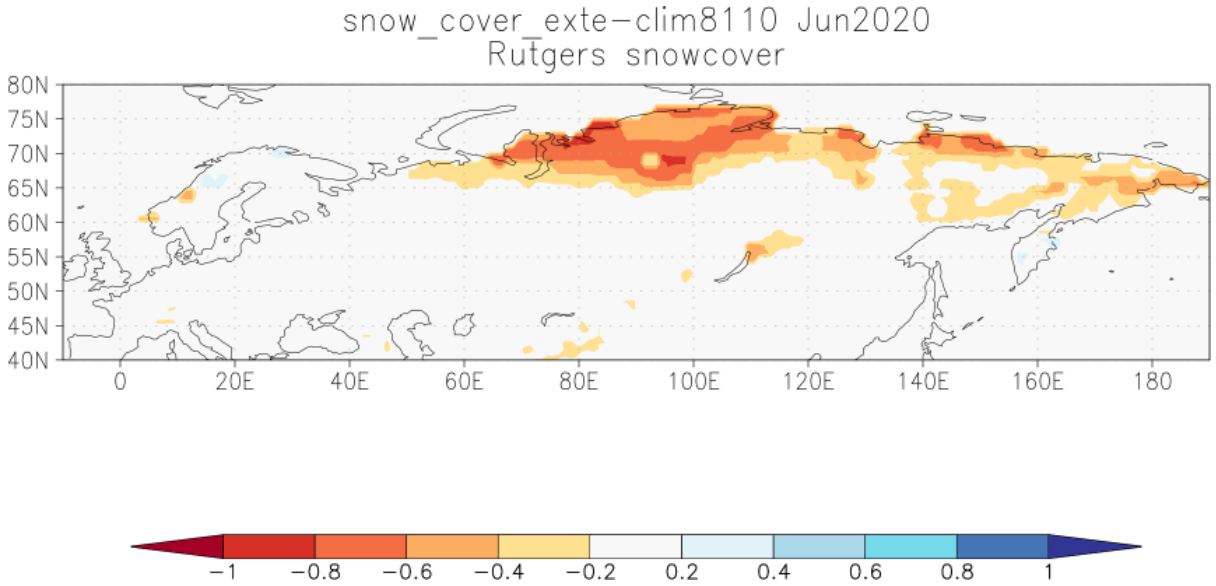

Figure 4: Snow cover anomalies (w.r.t. 1981-2010) [fract.] in June 2020, the low snow cover is caused by the preceding warm months and enables much higher temperatures in June.

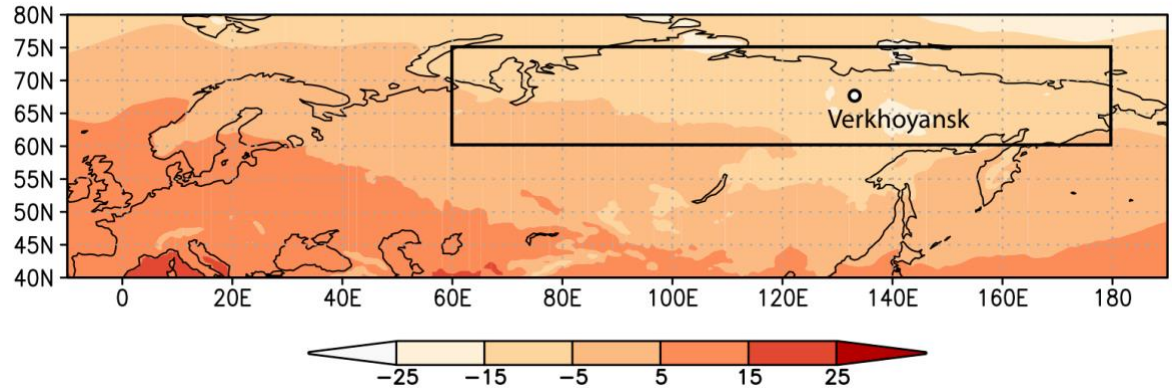

Figure 5: ERA5 near surface (T2m) temperature [°C] Jan-Jun climatology for 1981-2010. The rectangle represents the study region at 60-75°N, 60-180°E.

To investigate potential trends in the frequency of occurrence of prolonged Siberian high temperatures, similar to the first half of 2020 (see Figure 1), we choose to analyse January-June averaged 2-m temperature over land in the region 60-75 ºN, 60-180 ºE. This region covers most of Siberia and includes the area affected by the 2020 spring monthly anomalies and Verkhonyansk, the station where the daily maximum temperature record was broken in June. The region is chosen to be representative of Siberia and, to avoid selection bias, is deliberately broader than the region that experienced the highest Jan-Jun temperatures in 2020. The January-June climatological mean temperatures are also relatively homogeneous across the study region (Figure 5).

To investigate if human-induced climate change played a role in increasing the likelihood of the record breaking temperature at the station Verkhonyansk, we analyse June maximum value of daily maximum 2-m temperature, hereafter referred to as June TXx, at the location of the station Verkhonyansk. Rather than analyse summer maxima, we restrict to the month of June because there is a strong seasonal cycle in temperature that peaks in July.

2 Data and methods

2.1 Statistical methods

In this study we analyse time series from observational gridded data sets and station data where long records of observed data are available. Next we analyse climate model output for the same quantities. We follow the WWA approach to attribution. The analysis steps include: (i) trend calculation from observations; (ii) model validation; (iii) multi-method multi-model attribution and (iv) synthesis of the attribution statement. The methods for the statistical analysis of temperature extremes, model evaluation and the synthesis are explained here.

Following this method we perform an attribution analysis for two event definitions, but also for two different periods in time for each model dataset: using data up to the event year, 2020, to attribute the current event and using data up to 2050 to answer the question how such events are likely to evolve further in the future. The probability ratios (explained here) for 2020 and 2050 are both given with respect to 1900.

2.2 Observational data

2.2.1 Verkhoyansk station data

The meteorological station Verkhoyansk (67.55°N, 133.38°E) is located in the area of the local airport at the absolute elevation of 138 meters. The station was established in 1869 and provides continuous observations until now. Before 1926 the number of data gaps was quite large. Starting from 1926 8-time observations were regularly taken with the number of gaps being typically below 10% and most occurring in winter time. This allows for quite an accurate record of daily mean, minimum and maximum temperatures. In September 1999 the station was relocated some 2.5 km southwestward from the airport. This did not result in any critical change in the station elevation (about 4 meters). In the earlier times two other major relocations were documented, specifically in October 1940 (by 1.5 km northward from its original location) and in April 1947 (by about 2.5 km southward to the airport area). Overall, the station should be considered as properly exposed, not influenced by any large infrastructure and providing a homogenous temperature record. Due to the large number of data gaps before 1926, we chose to analyse June TXx from 1926 onwards (Figure 6).

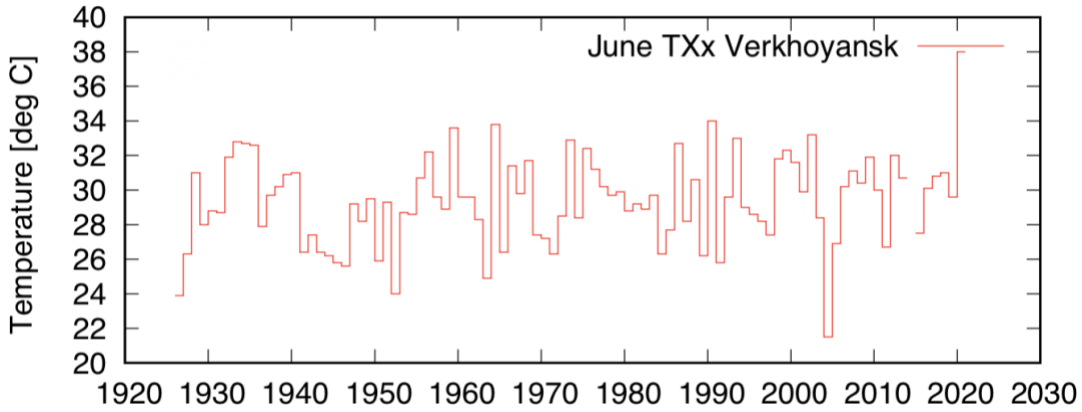

Figure 6: The series of June TXx Verkhoyansk observed temperatures analysed in this study

2.2.2 Gridded datasets

For the assessment of the large region we use two gridded datasets: ERA5, which is the latest global reanalysis product from ECMWF over 1979–2020 and GISTEMP 250km anomalies (with respect to 1951 - 1980), from the National Aeronautics and Space Administration (NASA) Goddard Institute for Space Science (GISS) surface temperature analysis (Hansen et al., 2010).

2.2.2 GMST

As a measure of anthropogenic climate change we use the (low-pass filtered) global mean surface temperature (GMST), where GMST is taken from the National Aeronautics and Space Administration (NASA) Goddard Institute for Space Science (GISS) surface temperature analysis (GISTEMP, Hansen et al., 2010).

2.3 Model and experiment descriptions

To attribute the observed changes to anthropogenic emissions of greenhouse gases and aerosols we use the following climate models. Because we analyse large-scale temperature extremes, especially in the January–June Siberian mean, we can include models with relatively low resolutions.

EC-Earth
EC-Earth (Hazeleger et al., 2012) is a coupled atmosphere-ocean model with a resolution of T159 (about 125 km). It is a 16-member ensemble of continuous simulations from 1860-2100 and is used as per the CMIP5 historical setup until 2005 and as per the RCP8.5 scenario from 2006.

MPI-ESM1-2-HR
The MPI-ESM1-2-HR earth system model was developed by the Max Planck Institute for Meteorology (Mauritsen et al., 2019, Mueller et al., 2018). It is a coupled global climate model. Here an ensemble of 10 CMIP6 realizations in the HR resolution (atmosphere spectral T127, roughly 100km grid size, on 95 vertical levels) is analysed. The historical experiment is available on ESGF for 1850-2014. For the period 2015-2100 the SSP3-7.0 scenario was used. Based on the model output variable Tx (daily maximum temperature), the June TXx was computed, in addition to the average January-June temperature for the Siberian region based on the model output variable daily mean temperature.

HadGEM3-A
Hadley Center Atmosphere and JULES land model with prescribed sea surface temperatures and sea ice concentrations. Horizontal resolution N216 is ~60km mid-latitudes with 85 vertical levels including resolved stratosphere. Data available from 1960 onwards with 15 ensemble members 1960 - 2013 and larger ensembles thereafter for both historical and historicalNat attribution experiments. (Ciavarella et al., 2018). The historical experiment uses RCP4.5 climate forcings after 2005.

CMIP5
CMIP5 is a set of global climate models, developed by several institutes around the world (Taylor et al., 2012). Here a subset of CMIP5 models passing the validation steps are used, with historical and RCP8.5 experiments together spanning the period between 1850 and 2100. The list of models used is given in the validation tables section.

CMIP6
Data from the 6th Coupled Model Intercomparison Project (CMIP6; Eyring et al., 2016) is also assessed. Therefore, we combine the historical simulations (1850 to 2015) with the shared socioeconomic pathways (SSPs) projections (O'Neill et al., 2016) for the years 2016 to 2100. Here, we only use data from SSP5-8.5. Models are excluded if they do not provide the relevant variables, do not run from 1850 to 2100, or include duplicate time steps or missing time steps. All available ensemble members are used.

For the regional analysis 38 models (200 ensemble members) are used that passed the validation tests and for Verkhoyansk 28 models (166 ensemble members).

SMILES
Single model initial-condition large ensembles (SMILEs) are large ensembles of mostly CMIP5-class models. While the model versions of the SMILEs are almost all included in the standard CMIP5 archive described above, the main benefit of the SMILEs is their larger sample size. This enables fitting distributions to the data at a given time step, rather than having to fit a distribution over time, which requires subtracting an estimate of the forced response first. The SMILEs have varying ensemble sizes (16 to 100, totalling 286 simulations of historical and RCP 8.5) and are centrally archived in the Multi Model Large Ensemble Archive (http://www.cesm.ucar.edu/projects/community-projects/MMLEA/). Details and references on the archive can be found in Deser et al. (2020).

MPI-GE
The Max Planck Institute for Meteorology Grand Ensemble (MPI-GE) is an ensemble of 100 realisations of the Max Planck Institute Earth System Model in the low resolution set up (MPI-ESM1.1), run with varying initial conditions (Maher et al., 2019). Monthly data are available on the ESGF. For 1850-2004 data from the historical experiment, and for 2005-2100 from the RCP8.5 scenario were downloaded and the January-June mean temperature for the siberian region calculated.

3 Observational analysis: return time and trend

The observational analysis of the station data is associated with very large uncertainties rendering the interpretation of the attribution results difficult. Confidence is much higher in the assessment over the large region where both data sets used give very similar results. Below the results of the assessment are given in tabular form with the first table representing the parameters of the distribution and the second table the trend assessment and changes in intensity and probability.

3.1 Verkhoyansk station

To fit a GEV to the station data we apply two slightly different statistical methods to the same underlying data to investigate the sensitivity of the result to the fit. The first method is the main WWA method (fit shown in Figure 7) and the second method is from MeteoFrance (denoted MF). Both are described in the methods document. As the best estimate return time of the 2020 event was undefined we use the rounded value of the lower bound return time of 140 years with which to define the station event.

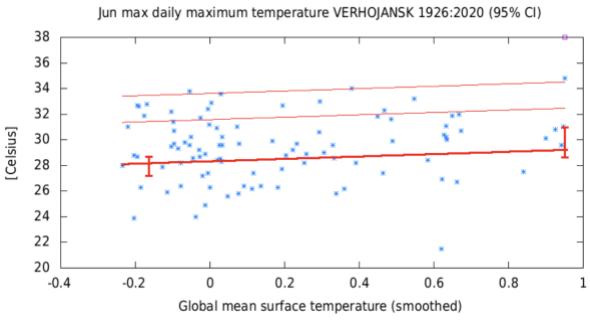

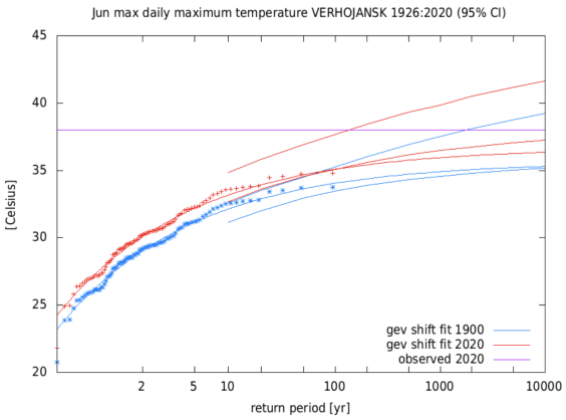

Figure 7: (a) June TXx observations from Verkhoyansk station (blue stars), fitted position parameter (thick red line), the 6 and 40 year return values (thin red lines) and the 2020 event (magenta square). Vertical bars indicate the 95\% confidence interval for the position parameter at the two reference years 2020 and 1900. (b) GEV fit. The data is plotted twice, being shifted with smoothed global mean temperature up to 2020 (red data points and fit with confidence interval) and down to 1900 (blue data points and fit with confidence interval), with the magnitude of the 2020 event shown as a horizontal magenta line.

Table 1: Statistical distribution and fitted parameters for Verkhoyansk station observations.

Dataset	Statistical model	Shift or scale?	Sigma	Shape
VERHOJANSK (1926 - 2019) WMO: 24266	GEV	shift	2.51 (1.885 ... 2.586)	-0.366 (-0.31 ... -0.117)
VERHOJANSK (1926 - 2020) WMO: 24266 (MF method)	GEV	shift	2.67 (2.33 ... 3.1)	-0.27 (-0.32 ... -0.21)

Table 2: Results of statistical analysis of Verkhoyansk station observations.

Dataset	Event magnitude	Return period	Ypast - Ynow	Probability RatioPR	Change in intensity ΔI [°C]
VERHOJANSK (1926 - 2019) WMO: 24266	38 °C	undefined (140.39 ... 325530000)	1900 - 2020	undefined (2.8055 ... inf)	1.041 (0.352 ... 3.368)
VERHOJANSK (1926 - 2020) WMO: 24266 (MF method)	38 °C	inf (7.29 ... inf)	1900 - 2020	inf (7.29 ... inf)	1.63 (1 ... 2.29)

3.2 Siberian region

The covariate approach was applied first to ERA5 reanalysis (beginning 1979, as per the Methods above) with a Gaussian parametric fit returning a scale parameter shown in Table 3 and return period for the Siberian region Jan-June 2020 mean shown in Table 4, along with the event magnitude in this dataset and results for the Probability Ratioof the 2020 event and associated shift of the distribution (Figure 8). The figure shows that the Gaussian distribution describes the data well. For the return period of the 2020 event the best estimate and both bounds are well defined and so we choose the rounded best estimate of 130 years as the threshold with which to define the large scale event.

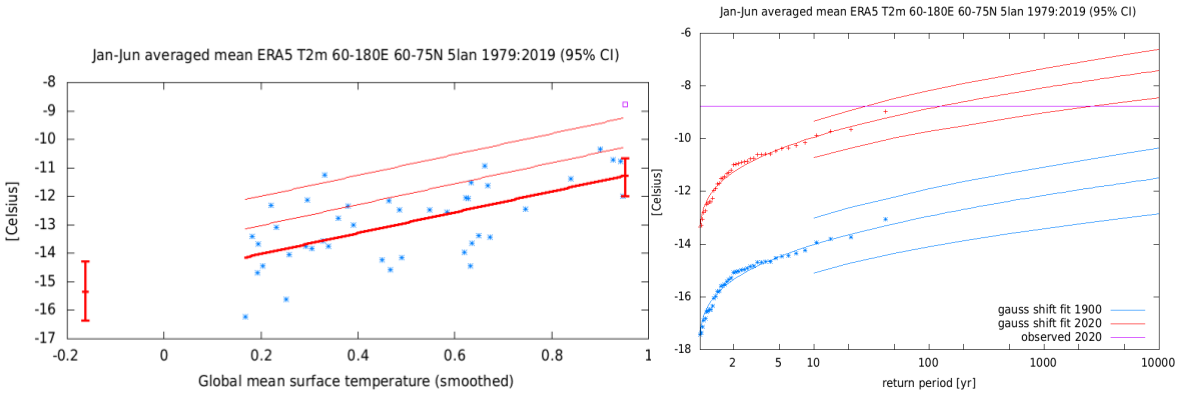

Figure 8: (a) Jan - June average temperature over Siberian region from ERA5 (blue stars), fitted position parameter (thick red line), the 6 and 40 year return values (thin red lines) and the 2020 event (magenta square). Vertical bars indicate the 95\% confidence interval for the position parameter at the two reference years 2020 and 1900. (b) Guassian fit. The data is plotted twice, being shifted with smoothed global mean temperature up to 2020 (red data points and fit with confidence interval) and

down to 1900 (blue data points and fit with confidence interval), with the magnitude of the 2020 event shown as a horizontal magenta line.

We compared the reanalysis product with the same method applied to the longer GISS 250km anomaly dataset (anomalies to 1951 - 1980). As the value for the 2020 event was not yet available in GISS we mapped the ERA5 2020 value to a GISS anomaly value by linear regression. The regression between ERA5 and GISS anomalies has a correlation coefficient r = 0.996, providing strong support for such a mapping approach. The results are presented also in Tables 4 & 5. Gaussian scale parameter, return period, PR and intensity changes from the different datasets are all consistent with one another.

Table 3: Statistical distribution and fitted parameters for Siberian region observations.

Dataset	Statistical model	Shift or scale?	Sigma
ERA5 (1979 - 2019)	Gaussian	shift	1.036 (0.826 ... 1.197)
GISS 250km anomalies (1916-2019)	Gaussian	shift	1.077 (0.917 ... 1.2)

Table 4: Results of statistical analysis of Siberian region observations.

Dataset	Event magnitude	Return period	Ypast - Ynow	Probability RatioPR	Change in intensity ΔI [°C]
ERA5 (1979 - 2020)	-8.759 °C	130.03 (28.566 ... 2802.3)	1900 - 2020	77268000 (22495 ... 158670000000000)	4.081 (2.417 ... 5.554)
GISS 250km anomalies (1916-2020)	5.7131 °C	316.43 (80.732 ... 3089.7)	1900 - 2020	81976 (3581.6 ... 10550000)	2.846 (2.142 ... 3.516)

4 Model validation

The climate models (see description in Section 2.3) were put through a rigorous model validation scheme before being included in the attribution analysis of June TXx at Verkhoyansk station and mean Jan-Jun temperatures in the Siberian region. The models were assessed according to the criteria laid out in the methods document to determine whether they are fit for purpose and can represent the extreme event well, allowing for a constant bias correction. To this end the seasonal cycle of modelled temperature was compared to the observed seasonal cycle of the Siberian region and Verkhoyansk station. Furthermore, the spatial pattern of observed and modelled climatology were compared. Lastly, the fit parameters of the statistical distribution were compared with the observed fit parameters.

For the attribution analysis of June TXx at Verkhoyansk station, 33 out of 55 considered models were used (Table A1, Appendix), being those which were evaluated to be “good” (the best estimate of the fit parameter for the models is within the confidence interval of the observed parameter estimate) or “reasonable” (the confidence intervals of model and observed parameters estimates overlap, but the best guess of the models is outside the 95% confidence interval in the observations). One further model (MIROC-ES2L) was excluded for possessing a trend that was both inconsistent with the observed trend and also did not include any processes that could plausibly explain this discrepancy and was thus considered unphysical. We chose to include also the “reasonable” models because only 7 models from a single category (CMIP5) evaluated to “good”, which would have provided little exploration of model uncertainty.

For the Siberian region 50 out of 71 models achieved a “good” evaluation (Table A2, Appendix), which was judged a sufficient sample on which to conduct the attribution analysis.

5 Multi-method multi-model attribution

This section shows probability ratios *PR* and change in intensity *ΔI* for all models that passed the validation and also includes the values calculated based on the observations. The synthesis of model- and observation-based results are discussed in Section 6.

5.1 Verkhoyansk station

Table 5: Results of the attribution analysis of the record-breaking high June temperature at Verkhoyansk station, comparing the event to a 1900 climate, as well as comparing future events of similar magnitudes to a 1900 climate.

Model / Observations	Threshold for return period 140 yr	Ypast - Ynow	Probability RatioPR	Change in intensity ΔI	Ypast - Yfuture	Probability RatioPR	Change in intensity ΔI
VERHOJANSK (1926 - 2020) WMO: 24266	38 °C	1900 - 2020	undefined (2.8055 ... undefined)	1.041 (0.352 ... 3.368)			
VERHOJANSK (1926 - 2020) WMO: 24266 (MF method)	38 °C	1900 - 2020	inf (7.29 ... inf)	1.63 (1 ... 2.29)			
CMCC_CMCC-CMS	25.69	1900 - 2020	18.68 (4.75 ... inf)	1.26 (0.99 ... 1.52)	1900 - 2050	104.17 (17.36 ... inf)	2.72 (2.16 ... 3.28)
CNRM-CERFACS_CNRM-CM5	34.05	1900 - 2020	7.75 (4.67 ... 15.06)	1.3 (1.06 ... 1.54)	1900 - 2050	25.57 (12.73 ... 60.31)	2.39 (1.95 ... 2.82)
CSIRO-BOM_ACCESS1-0	34.95	1900 - 2020	10.42 (4.48 ... 83.61)	1.35 (1.1 ... 1.62)	1900 - 2050	44.29 (13.82 ... 501.33)	2.67 (2.19 ... 3.19)
CSIRO-BOM_ACCESS1-3	29.46	1900 - 2020	14.42 (5.59 ... inf)	1.06 (0.85 ... 1.31)	1900 - 2050	85.71 (24.03 ... inf)	2.38 (1.91 ... 2.9)
CSIRO-QCCCE_CSIRO-Mk3-6-0	27.6	1900 - 2020	7.51 (5.45 ... 11.75)	1.08 (1 ... 1.17)	1900 - 2050	33.29 (21.57 ... 59.14)	2.32 (2.16 ... 2.47)
IPSL_IPSL-CM5A-LR	28.2	1900 - 2020	inf (1239.07 ... inf)	2.08 (1.96 ... 2.21)	1900 - 2050	inf (10113.92 ... inf)	3.68 (3.48 ... 3.89)
IPSL_IPSL-CM5B-LR	28.94	1900 - 2020	inf (146.73 ... inf)	1.67 (1.46 ... 1.9)	1900 - 2050	inf (855.31 ... inf)	2.94 (2.56 ... 3.34)
MRI_MRI-CGCM3	35.71	1900 - 2020	3.76 (2.36 ... 8.39)	0.97 (0.7 ... 1.21)	1900 - 2050	11.42 (5.29 ... 36.26)	2.05 (1.48 ... 2.57)
NASA-GISS_GISS-E2-H	33.33	1900 - 2020	19.42 (6.24 ... inf)	1.89 (1.59 ... 2.18)	1900 - 2050	70.75 (17.07 ... inf)	3.13 (2.62 ... 3.63)

NASA-GISS_GISS-E2-R	32.85	1900 - 2020	10.07 (4.39 ... 74.74)	1.74 (1.39 ... 2.07)	1900 - 2050	25.18 (8.85 ... 261.42)	2.65 (2.12 ... 3.15)
HadGEM3-A	30.819	1900 - 2020	103000000 (132.02 ... inf)	3.272 (2.178 ... 4.17)	1900 - 2050	(...)	(...)
ACCESS-CM2 (2)	25.772	1900 - 2020	inf (11.11 ... inf)	1.98 (0.83 ... 3.12)	1900 - 2050	inf (inf ... inf)	(...)
ACCESS-ESM1-5 (3)	27.13	1900 - 2020	inf (16.78 ... inf)	2.02 (1.23 ... 2.81)	1900 - 2050	inf (491.56 ... inf)	(...)
AWI-CM-1-1-MR (1)	37.406	1900 - 2020	inf (9.29 ... inf)	3.8 (1.56 ... 5.87)	1900 - 2050	inf (14.66 ... inf)	(...)
CMCC-CM2-SR5 (1)	27.939	1900 - 2020	inf (9.67 ... inf)	3.71 (2.31 ... 5.09)	1900 - 2050	inf (118.11 ... inf)	(...)
CNRM-CM6-1 (1)	28.596	1900 - 2020	6.19 (0.6 ... inf)	0.94 (-0.21 ... 2)	1900 - 2050	inf (16.15 ... inf)	(...)
CNRM-CM6-1-HR (1)	31.628	1900 - 2020	28.61 (0.97 ... inf)	1.6 (-0.03 ... 3.26)	1900 - 2050	inf (11.74 ... inf)	(...)
CNRM-ESM2-1 (1)	31.56	1900 - 2020	7.13 (1.86 ... inf)	1.72 (0.58 ... 2.79)	1900 - 2050	10.38 (2.02 ... inf)	(...)
CanESM5 (50)	27.837	1900 - 2020	inf (inf ... inf)	3.35 (3.11 ... 3.6)	1900 - 2050	inf (inf ... inf)	(...)
EC-Earth3 (3)	30.096	1900 - 2020	inf (120.51 ... inf)	2.98 (1.78 ... 4.19)	1900 - 2050	inf (inf ... inf)	(...)
FGOALS-g3 (3)	35.845	1900 - 2020	2795.4 (15.04 ... inf)	2.24 (1.34 ... 3.24)	1900 - 2050	inf (132.72 ... inf)	(...)
GFDL-CM4 (1)	29.478	1900 - 2020	6.81 (0.35 ... inf)	1.2 (-0.56 ... 2.94)	1900 - 2050	1.67 (0.28 ... 838234.7)	(...)
GFDL-ESM4 (1)	25.115	1900 - 2020	6.21 (0 ... inf)	0.52 (-0.68 ... 1.84)	1900 - 2050	inf (520.88 ... inf)	(...)
HadGEM3-GC31-LL (4)	28.65	1900 - 2020	946.91 (14.26 ... inf)	2.33 (1.47 ... 3.13)	1900 - 2050	inf (inf ... inf)	(...)
HadGEM3-GC31-MM (3)	33.144	1900 - 2020	2.51 (1.4 ... 4.72)	1.44 (0.54 ... 2.34)	1900 - 2050	32.43 (11.28 ... 133.27)	(...)
INM-CM5-0 (1)	28.265	1900 - 2020	inf (0.55 ... inf)	1.49 (-0.2 ... 3.21)	1900 - 2050	inf (713.31 ... inf)	(...)
IPSL-CM6A-LR (6)	31.568	1900 - 2020	6.71 (2.1 ... 61.87)	1.27 (0.52 ... 1.99)	1900 - 2050	548017350 (97.91 ... inf)	(...)
MIROC6 (50)	29.932	1900 - 2020	22.24 (11.84 ... 42.21)	1.16 (0.94 ... 1.36)	1900 - 2050	inf (inf ... inf)	(...)
MPI-ESM1-2-HR (2)	36.249	1900 - 2020	14.13 (1.73 ... inf)	2.06 (0.49 ... 3.56)	1900 - 2050	9.18 (1.62 ... 589.3)	(...)
MPI-ESM1-2-LR (10)	28.727	1900 - 2020	336.74 (17.58 ... inf)	1.87 (1.28 ... 2.46)	1900 - 2050	inf (inf ... inf)	(...)

MRI-ESM2-0 (2)	36.307	1900 - 2020	25.16 (1.87 ... inf)	1.62 (0.37 ... 2.83)	1900 - 2050	inf (51.61 ... inf)	(...)
NESM3 (1)	26.558	1900 - 2020	15.34 (1.48 ... inf)	2.56 (0.31 ... 4.68)	1900 - 2050	3123.42 (7.63 ... inf)	(...)
UKESM1-0-LL (5)	28.97	1900 - 2020	6.18 (2.64 ... 15.39)	1.81 (0.98 ... 2.62)	1900 - 2050	2645235120000 (5348.56 ... inf)	(...)

5.2 Siberian region

Table 6: Results of the attribution analysis of the prolonged heat in the Siberian region, comparing the event to a 1900 climate, as well as comparing future events of similar magnitudes to a 1900 climate.

Model / Observations	Threshold for return period 130 yr [°C]	Ypast - Ynow	Probability RatioPR	Change in intensity ΔI [°C]	Ypast - Yfuture	Probability RatioPR	Change in intensity ΔI [°C]
ERA5 (1979 - 2020)	-8.759 °C	1900 - 2020	77268000 (22495 ... 158670000000000)	4.081 (2.417 ... 5.554)			
GISS 250km anomalies	5.7131 °C	1900 - 2020	81976 (3581.6 ... 10550000)	2.846 (2.142 ... 3.516)			
MPI-ESM1.2-HR (10)	-8.383	1900 - 2020	5157 (2172.3 ... 10824)	2.417 (2.192 ... 2.542)	1900 - 2050	114610 (52172 ... 242490)	3.913 (3.727 ... 4.081)
BCC_bcc-csm1-1-m	-7.75	1900 - 2020	109016.66 (37772.48 ... 408410.81)	2.72 (2.57 ... 2.88)	1900 - 2050	3328189.32 (987395.36 ... 14261378.66)	4.35 (4.14 ... 4.56)
BNU_BNU-ESM	-12.67	1900 - 2020	349475471.83 (34086945.87 ... 6166280784.11)	4.11 (3.94 ... 4.29)	1900 - 2050	31275151496.14 (2710147277.79 ... 606075303240.33)	6.99 (6.74 ... 7.23)
CMCC_CMCC-CESM	-13.3	1900 - 2020	475.85 (207.2 ... 1221.83)	1.76 (1.62 ... 1.9)	1900 - 2050	23692.74 (8637.52 ... 72287.7)	3.92 (3.71 ... 4.13)
CMCC_CMCC-CMS	-12.01	1900 - 2020	1027.34 (461.94 ... 2622.24)	1.96 (1.85 ... 2.08)	1900 - 2050	55815.48 (21644.69 ... 172007.66)	4.24 (4.05 ... 4.46)
CNRM-CERFACS_CNRM-CM5	-13.55	1900 - 2020	6400.76 (4050.22 ... 11345.34)	2.43 (2.36 ... 2.53)	1900 - 2050	257456.1 (153370.76 ... 474742.24)	4.47 (4.38 ... 4.58)
CSIRO-BOM_ACCESS1-0	-9.78	1900 - 2020	3583.94 (1833.78 ... 9089.35)	2.5 (2.38 ... 2.66)	1900 - 2050	179537.85 (79407.21 ... 501784.59)	4.96 (4.75 ... 5.19)
CSIRO-BOM_ACCESS1-3	-8.45	1900 - 2020	1851.25 (889.12 ... 4469.25)	2.05 (1.93 ... 2.18)	1900 - 2050	128529.22 (55978.8 ... 339380.17)	4.57 (4.37 ... 4.78)
FIO_FIO-ESM	-10.75	1900 - 2020	334.42 (201.15 ... 596.89)	1.61 (1.54 ... 1.68)	1900 - 2050	4761.13 (2493.98 ... 9548.91)	2.77 (2.65 ... 2.89)
INM_inmcm4	-9.48	1900 - 2020	859.4 (380.86 ... 2464.4)	1.87 (1.74 ... 1.99)	1900 - 2050	21620.28 (7916.15 ... 79429.64)	3.43 (3.21 ... 3.63)

IPSL_IPSL-CM5A-LR	-8.52	1900 - 2020	229787.88 (108683.52 ... 548418.33)	2.51 (2.44 ... 2.59)	1900 - 2050	13319339.61 (5846617.82 ... 34725830.68)	4.44 (4.34 ... 4.54)
IPSL_IPSL-CM5A-MR	-7.1	1900 - 2020	38099.22 (14740.45 ... 125396.22)	2.18 (2.08 ... 2.29)	1900 - 2050	1950219.5 (649609.24 ... 7397378.47)	3.96 (3.79 ... 4.13)
MIROC_MIROC-ESM-CHEM	-9.89	1900 - 2020	376026794.01 (35097379.79 ... 9904336716.06)	3.8 (3.66 ... 3.98)	1900 - 2050	46974628761.99 (4163914971.46 ... 1276608970267.47)	7.61 (7.39 ... 7.84)
MIROC_MIROC-ESM	-9.63	1900 - 2020	14690116.44 (2754617.4 ... 119119789.32)	3.55 (3.4 ... 3.73)	1900 - 2050	1643668973.54 (292485620.53 ... 13914772142.24)	6.94 (6.72 ... 7.17)
MIROC_MIROC5	-11.64	1900 - 2020	27914.24 (13811.83 ... 68475.76)	2.42 (2.32 ... 2.55)	1900 - 2050	1714170.06 (785785.91 ... 4483455.02)	4.62 (4.49 ... 4.76)
MPI-M_MPI-ESM-MR	-8.24	1900 - 2020	77916.1 (29817.83 ... 269695.66)	2.99 (2.86 ... 3.15)	1900 - 2050	3094325.79 (1024242.05 ... 12206162.06)	5.06 (4.85 ... 5.28)
MRI_MRI-CGCM3	-10.55	1900 - 2020	128.06 (77.3 ... 241.85)	1.65 (1.54 ... 1.78)	1900 - 2050	3363.92 (1700.61 ... 7814.05)	3.5 (3.27 ... 3.74)
NASA-GISS_GISS-E2-H-CC	-10.22	1900 - 2020	519844.65 (96020.82 ... 5191824.61)	2.8 (2.64 ... 2.97)	1900 - 2050	18876850.06 (2891642.34 ... 238869471.96)	4.45 (4.21 ... 4.68)
NASA-GISS_GISS-E2-H	-9.78	1900 - 2020	432483.4 (176611.48 ... 1243253.83)	2.61 (2.53 ... 2.73)	1900 - 2050	19608930.67 (7265526.97 ... 60235112.47)	4.34 (4.21 ... 4.47)
NASA-GISS_GISS-E2-R	-10.68	1900 - 2020	7697.5 (3934.54 ... 16458.92)	1.99 (1.9 ... 2.09)	1900 - 2050	114459.43 (52260.12 ... 278965.66)	3.03 (2.89 ... 3.17)
NCAR_CCSM4	-10.39	1900 - 2020	75048.62 (41686.78 ... 144698.82)	3.15 (3.08 ... 3.26)	1900 - 2050	2538659.66 (1322783.9 ... 5128333.79)	5.18 (5.08 ... 5.29)
NCC_NorESM1-M	-11.8	1900 - 2020	5621.11 (2512.73 ... 15190.98)	2.66 (2.52 ... 2.81)	1900 - 2050	233163.6 (89455.08 ... 725074.14)	4.94 (4.72 ... 5.16)
NSF-DOE-NCAR_CESM1-BGC	-9.93	1900 - 2020	23189.75 (7546.63 ... 109379.49)	3.04 (2.87 ... 3.21)	1900 - 2050	678296.23 (190159.62 ... 3872978.88)	5.03 (4.77 ... 5.28)
HadGEM3-A ALL	-12.06	1900 - 2020	2361200 (146240 ... 68329000)	3.41 (2.86 ... 4.06)	1900 - 2050	(...)	(...)
AWI-CM-1-1-MR (1)	-7.574	1900 - 2020	14030.35 (687.19 ... 439020)	439020 (2.03 ... 3.44)	1900 - 2050	3579577050 (21845129.1 ... 1221722830000)	4.86 (4.26 ... 5.46)
BCC-CSM2-MR (1)	-9.962	1900 - 2020	471.1 (47.1 ... 5868.6)	5868.6 (1.12 ... 2.4)	1900 - 2050	282823902 (3075592.16 ... 48481837100)	4.2 (3.63 ... 4.78)
CESM2 (5)	-7.59	1900 - 2020	63089.58 (14487.54 ... 315955.59)	315955.59 (2.94 ... 3.59)	1900 - 2050	11220208200 (1017963800 ... 138662239000)	5.61 (5.31 ... 5.91)
CESM2-WACCM (3)	-9.024	1900 - 2020	16768.21 (3225.11 ... 103297.11)	2.79 (2.42 ... 3.16)	1900 - 2050	2635871170 (144754117 ... 57141801500)	4.97 (4.61 ... 5.31)
CIESM (1)	-9.905	1900 - 2020	29.11 (3.11 ... 275.36)	1.25 (275.36 ... 2.06)	1900 - 2050	695.57 (68.71 ... 8193.69)	2.15 (1.46 ... 2.83)
CMCC-CM2-SR5 (1)	-9.23	1900 - 2020	469151.97 (13776.54 ... 27819549.5)	3.18 (2.63 ... 3.72)	1900 - 2050	7806252650000000 (2379992540000 ... 1020451130000000 00000)	6.62 (5.99 ... 7.23)

CNRM-CM6-1-HR (1)	-10.418	1900 - 2020	10098.68 (437.49 ... 315195.18)	10098.68 (315195.18 ... 3.05)	1900 - 2050	35443181600 (151606194 ... 25362255800000)	4.87 (4.25 ... 5.48)
CanESM5 (50)	-7.432	1900 - 2020	134473.15 (79965.55 ... 223437.51)	134473.15 (223437.51 ... 3.52)	1900 - 2050	155126591000000 (53282991600000 ... 449637340000000)	6.87 (6.78 ... 6.96)
CanESM5-CanOE (3)	-7.72	1900 - 2020	104703.24 (13061.39 ... 1025559.75)	3.32 (2.83 ... 3.78)	1900 - 2050	138593564000000 (1968567690000 ... 1443625090000000)	6.77 (6.39 ... 7.18)
EC-Earth3 (7)	-11.092	1900 - 2020	864766.8 (205824.01 ... 3759569.21)	864766.8 (3759569.21 ... 3.5)	1900 - 2050	274833638000000 (15687565500000 ... 5837131710000000)	6.09 (5.87 ... 6.31)
EC-Earth3-Veg (4)	-10.87	1900 - 2020	3323104.59 (484670.15 ... 28209229.96)	3.28 (3.04 ... 3.53)	3.53 - 2050	657934104000000 (14412277500000 ... 3908888200000000)	5.98 (5.73 ... 6.24)
FGOALS-f3-L (1)	-12.515	1900 - 2020	1287.81 (93.35 ... 23213.61)	1287.81 (23213.61 ... 3.09)	3.09 - 2050	991540124 (7443665.77 ... 205393237000)	5.14 (4.46 ... 5.84)
FGOALS-g3 (4)	-13.724	1900 - 2020	36972.49 (7296.8 ... 200192.58)	2.83 (2.51 ... 3.15)	1900 - 2050	413274996 (41524226.4 ... 4855558040)	4.4 (4.12 ... 4.68)
FIO-ESM-2-0 (3)	-10.406	1900 - 2020	105821.55 (13287.24 ... 989541.44)	105821.55 (989541.44 ... 3.87)	1900 - 2050	2955730750 (166029062 ... 72304549500)	5.45 (5.04 ... 5.86)
GFDL-CM4 (1)	-10.953	1900 - 2020	279167.26 (8047.34 ... 14790299.7)	2.82 (2.23 ... 3.42)	1900 - 2050	4044132030000000 (1891764020000 ... 27850197600000000000)	5.98 (5.44 ... 6.54)
GFDL-ESM4 (1)	-9.868	1900 - 2020	21.62 (3.71 ... 120.94)	21.62 (120.94 ... 1.24)	1900 - 2050	878680.05 (33238.12 ... 35559254.2)	2.53 (2.11 ... 2.94)
HadGEM3-GC31-LL (4)	-11.489	1900 - 2020	37360.52 (7614 ... 208395.23)	37360.52 (208395.23 ... 2.74)	1900 - 2050	23630039500000 (791620476000 ... 946091201000000)	5.38 (5.12 ... 5.65)
HadGEM3-GC31-MM (3)	-11.466	1900 - 2020	308.05 (81.62 ... 1127.66)	1.55 (1.21 ... 1.89)	1900 - 2050	107727278000 (4009022080 ... 3653994640000)	4.69 (4.37 ... 5.01)
INM-CM4-8 (1)	-11.076	1900 - 2020	71.8 (8.47 ... 667.34)	71.8 (667.34 ... 1.63)	1900 - 2050	24064298.1 (417335.6 ... 2751496950)	3.16 (2.68 ... 3.63)
IPSL-CM6A-LR (6)	-8.987	1900 - 2020	33851.79 (8945.43 ... 140497.11)	33851.79 (140497.11 ... 3.02)	1900 - 2050	4588690190000 (298324221000 ... 84410690100000)	5.61 (5.36 ... 5.86)
MIROC6 (50)	-9.492	1900 - 2020	12671 (8277.73 ... 19659.39)	12671 (19659.39 ... 2.56)	1900 - 2050	1264371450000 (503891431000 ... 3224805860000)	4.8 (4.72 ... 4.87)
MPI-ESM1-2-HR (2)	-8.523	1900 - 2020	2097.08 (285.84 ... 17477.45)	2.28 (1.79 ... 2.26)	1900 - 2050	10047945.1 (559578.91 ... 247646638)	3.86 (3.41 ... 4.3)
MPI-ESM1-2-LR (10)	-9.814	1900 - 2020	6198.4 (2432.36 ... 15973.56)	6198.4 (15973.56 ... 2.78)	1900 - 2050	5128678180 (951888987 ... 28953417500)	4.73 (4.54 ... 4.92)
NorESM2-MM (1)	-11.012	1900 - 2020	122.63 (21.64 ... 786.05)	1.66 (1.09 ... 2.98)	1900 - 2050	435810.3 (18596.74 ... 15189481.98)	3.75 (3.1 ... 4.37)

UKESM1-0-LL (5)	-12.621	1900 - 2020	5774.56 (1698.12 ... 21228.96)	5774.56 (21228.96 ... 2.2)	1900 - 2050	5612837200000000 00 (946529685000000 0 ... 4500740100000000 0000)	6.81 (6.56 ... 7.06)
MPI-GE (100)	-8.572	1900 - 2020	26073 (20296 ... 31948)	2.858 (2.792 ... 2.862)	1900 - 2050	1444500 (1046300 ... 1828700)	4.991 (4.927 ... 4.994)

6 Hazard synthesis

For both event definitions we calculate the Probability Ratioas well as the change in magnitude of the event in the observations and the models. Only the models that have passed the evaluation above are included. We synthesise the assessment from the models with each other as well as with the observations to give an overarching attribution statement, following the same methodology as in Philip et al., 2018. First the observations are combined. As the natural variability is strongly correlated—they are based on the same observations over 1979–2020—we just average the best estimate values and lower and upper bounds for this. The difference is added as a representation uncertainty (white extensions on the light blue bars). In contrast, the natural variability in the models is uncorrelated, so we can compute a weighted average. However, as the spread of the models is larger than expected from natural variability alone, we add a model spread term to each model and the weighted average (white extensions on the light red bars) to account for systematic model errors. In the Probability Ratio, we run into the problem that the 2020 event often is above the upper bound of the probability distribution in 1900, indicating that the event would have been impossible in that climate. This is indicated by an arbitrary large value of 10_{33} for the probability ratio. The results including this value are not mathematically well-defined and so are intended merely to indicate the situation described above. Finally, observations and models are compatible, so they are combined into a single result in two ways. Firstly, we neglect model uncertainties beyond the model spread and compute the weighted average of models and observations: this is indicated by the magenta bar. Secondly, as model uncertainty can be larger than the model spread, we also show the more conservative estimate of an unweighted average of observations and models, indicated by the white box around the magenta bar in the synthesis figures.

6.1 The event compared to past climate

6.1.1 Verkhoyansk station

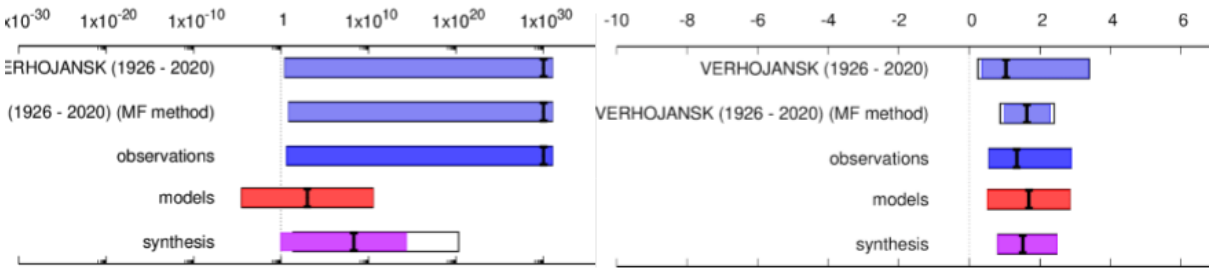

Figure 9: Synthesis of probability ratios (left) and changes in intensity (right) from the attribution analysis of June TXx at Verkhoyansk station. A figure including all models can be found in the appendix (Figure A1, Appendix).

An event like the extreme temperature of 20th of June 2020 at Verkhoyansk station with inclusion of reasonable models has a best estimate Probability Ratio(PR) of 210 million (but possibly still less than

1). While the PR results are of low confidence (encompassing “no change”) the results for the change in intensity confidently show an anthropogenic shift, best estimate being 1.5°C (0.8 - 2.5°C).
In the observations the best estimate and upper bound PR is infinite while the lower bound is 4.52.

The change of intensity estimated from observations is 1.34°C (0.56 - 2.9°C). The model synthesis intensity change of 1.7°C (0.52 - 2.9°C) is therefore consistent with the intensity change from observations and the model + observed synthesis values are 1.51°C (0.81 - 2.5°C).

The station does have a much smaller signal to noise than the large region - a standard deviation around the trend of around 2.5°C with a shift of only around 1.5°C means the uncertainties are large.The presence of an upper bound of the distribution close to the observed extreme will tend to produce large PR values for small shifts exacerbating the uncertainty in the Probability Ratio..

The weighting used to add model uncertainty in the synthesis makes it possible that models with divergent Probability Ratios are down-weighted unnecessarily by the algorithm, which assumes log-normal distributions, so that we could expect larger values to be closer to the truth. Removing the weighting for model uncertainty gives PR (good models) > 4600.

Table 7: Synthesis of probability ratios and changes in intensity from the attribution analysis of June TXx at Verkhoyansk station. The weighted average uncertainty range corresponds to the magenta bar, and the unweighted average uncertainty range to the white box, of the synthesis bar in Figure 9.

		Probability ration PR [-]					**Change in intensity [°C]**				
			Weighted average		**Unweighted average**			**Weighted average**		**Unweighted average**	
Dataset	**Ypast - Ynow**	**Best estimate**	**Lower bound**	**Upper bound**	**Lower bound**	**Upper bound**	**Best estimate**	**Lower bound**	**Upper bound**	**Lower bound**	**Upper bound**
VERHOJANSK (1926 - 2020)	1900 - 2020	1.00E+30	2.81	1.00E+31	2.81	1.00E+31	1.04	0.352	3.37	0.236	3.4
VERHOJANSK (1926 - 2020) (MF method)	1900 - 2020	1.00E+30	7.29	1.00E+31	7.29	1.00E+31	1.63	1	2.29	0.875	2.41
Observations average	1900 - 2020	1.00E+30	4.52	1.00E+31	4.52	1.00E+31	1.34	0.555	2.89	0.555	2.89
Models average	1900 - 2020	1.02E+03	3.22E-05	3.28E+10	3.22E-05	3.28E+10	1.69	0.518	2.85	0.518	2.85
synthesis	1900 - 2020	2.05E+08	0.937	2.23E+14	22.9	1.96E+20	1.51	0.809	2.48	0.809	2.48

6.1.2 Siberian region

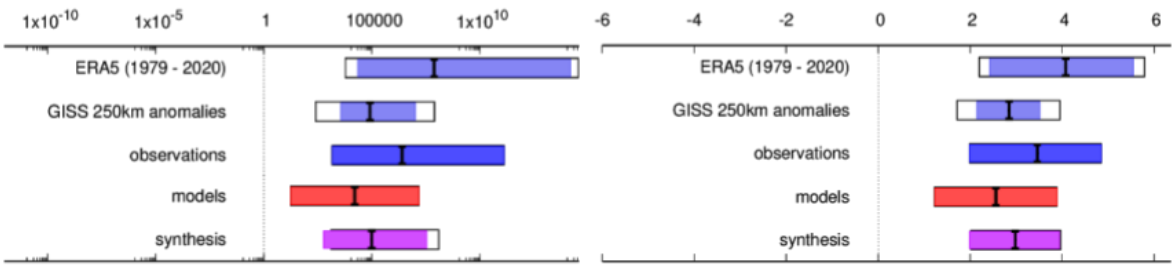

Figure 10: Synthesis of probability ratios (left) and changes in intensity (right) from the attribution analysis of Jan-Jun mean temperature in Siberian region, comparing the 2020 event with 1900 climate. A figure including all models can be found in the appendix (Figure A2, Appendix).

The synthesis of 50 good models and obs. is confident that PR is large, with a lower bound of almost 600 and best estimate around 99,000, making the event effectively impossible in the natural world. All 'good' models had the lower bounds of the PR estimates well above 1. There is a large degree of consistency between observational and model analyses for both PR and changes in intensity, so we have reason to be confident of the overall result. The observational average has a larger best estimate shift in intensity (around 3.5K) than the model average best estimate (around 2.5K), although the longer observational dataset (GISS) is closer to the models and the two values are well within each other's uncertainty estimates.

Table 8: Synthesis of probability ratios and changes in intensity from the attribution analysis of Jan-Jun mean temperature in Siberian region, comparing the 2020 event with 1900 climate. The weighted average uncertainty range corresponds to the magenta bar, and the unweighted average uncertainty range to the white box, of the synthesis bar in Figure 10.

		Probability ration PR [-]					**Change in intensity [°C]**				
			Weighted average		**Unweighted average**			**Weighted average**		**Unweighted average**	
Dataset	**Ypast - Ynow**	**Best estimate**	**Lower bound**	**Upper bound**	**Lower bound**	**Upper bound**	**Best estimate**	**Lower bound**	**Upper bound**	**Lower bound**	**Upper bound**
ERA5 (1979 - 2020)	1900 - 2020	7.73E+07	2.25E+04	1.59E+14	5.94E+03	3.49E+14	4.08	2.42	5.55	2.2	5.79
GISS 250km anomalies	1900 - 2020	8.20E+04	3.58E+03	1.06E+07	257	7.84E+07	2.85	2.14	3.52	1.72	3.95
Observations average	1900 - 2020	2.52E+06	1.49E+03	1.29E+11	1.49E+03	1.29E+11	3.46	1.99	4.85	1.99	4.85
Models average	1900 - 2020	1.63E+04	17.6	1.51E+07	17.6	1.51E+07	2.56	1.23	3.89	1.23	3.89
synthesis	1900 - 2020	9.93E+04	588	3.48E+07	1.30E+03	1.23E+08	2.98	1.99	3.94	2.02	3.97

A parallel analysis of 7 SMILES large ensembles was also conducted using a different method to the covariate approach. Instead the large ensemble values at 2020 could be used in a Gaussian parametric fit and compared with the same from an earlier epoch. Due to the shorter experiment length the date of 1950 was chosen in place of the 1900 baseline used for the rest of the analysis.

The SMILEs results gives a best estimate Probability Ratio(2020 to the 1950 baseline) of around 1500 (multi-model median) - 2200 (multi-model mean). The PR values for 2050 are an order of magnitude or more larger again, as would be anticipated. These values for both 2020 and 2050 would be even larger still if the analysis could be conducted to the same 1900 baseline as the models using the covariate approach.

Using this different method of analysis we would draw very similar conclusions regarding the change in likelihood of the regional Siberian heat and so this provides independent evidence for the near impossibility of this event in the natural world (Table 9).

Table 9: SMILES individual model values, mean and median PR

Model	**Probability Ratio** 2020 vs 1950	**Probability Ratio** 2050 vs 1950
CESM1-CAM5 (40)	1321	43886
CSIRO-Mk3-6-0 (30)	1488	70964
CanESM2 (50)	1733	135780
EC-EARTH (16)	1910	33668
GFDL-ESM2M (30)	7414	109580
GFDL-CM3 (20)	1367	22796
GFDL-CM3	314	33103
Mean	**2221**	**64254**
Median	**1488**	**43886**

6.2 Future

Different scenarios were used when modelling the future climate (see Section 2.3), however an analysis of the partition between model and scenario uncertainty in global mean surface temperatures at 2050 in the CMIP6 collection of coupled models indicates that scenario uncertainty still plays a small role compared to model uncertainty, responsible for perhaps 35% of the spread in GMST. These values can be read off from Figure 1 of Lehner et al, .2020.

6.2.1 Verkhoyansk station

Data and resources availability at such rapid time scales of the study meant we were unable to perform an analysis of the change in intensity and likelihoods for the station.

6.2.2 Siberian region

The best estimate synthesis Probability Ratioincreases by 2050, compared to 2020, by another 3 to 4 orders of magnitude, (from about 99,000) to 160 million, although the lower bound of the Probability Ratiois less than that for 2020 (see Figure A3, Appendix). Given that the probabilities of occurrence in the counterfactual are extremely small the uncertainties are so large, that the exact figures are not very reliable What is clear is that the Probability Ratiowill have increased further. The synthesis change of intensity for 2050 is 4.85°C (2.43 to 7.26°C) which is a 30 year increase in best estimates of around 1.9°C. In other words in 2050 a hot spell with a 1 in 140 return time would be expected to be about 2°C warmer.

7 Vulnerability and exposure

Whilst intense heatwaves are amongst the deadliest natural disasters facing humanity today (e.g., Harrington and Otto, 2020), prolonged above-average heat episodes can induce long-term environmental changes. The frequency and intensity of such heat episodes are on the rise globally, and Siberia is a region of the globe warming much faster than the global average.

Geographic Siberia is a sparsely populated but vast region, home to a population of more than 33 million people who mostly live in the south but there are also some small settlements north of the Arctic circle, such as the town Verkhoyansk (population: slightly over 1100) featured in this study. Economic activities around Verkhoyansk are mostly hunting and forestry. However, the area impacted by the heat also extends northward to the Arctic coast where the other economic sectors are developed and permafrost abounds.

Hot days in Siberia are not uncommon, however the population is not used to extreme heat and may be more likely to suffer from common heat-induced problems such as headaches and skin-conditions. Combined with other risk factors such as age, respiratory illnesses, cardiovascular disease, other pre-existing health conditions and socio-economic disadvantages, extreme heat impacts become even more acute (Kovats and Hajat 2008, McGregor et al 2015).

The Siberian environment on the other hand, is particularly vulnerable to prolonged above average heat. Prolonged heat waves clearly impact the local ecosystems, resulting in e.g. wildfires. These might expand over large areas affecting considerable loss of the resources for forestry. Moreover, wildfires emit continuous smoke which is rich in (low level) aerosols affecting air quality and also initiating important feedbacks with hot weather which can potentially enhance the temperature locally.

Increasing local temperatures also contribute to the thawing of permafrost covering most of Eastern Siberia. This loss of permafrost will be accelerated during heat events. A knock-on effect is the release of the greenhouse gas methane and the collapse of infrastructure. In terms of infrastructure, seasonal roads and their bearing capacity are affected, as well as buildings and industrial structures. For many years, the stability of the local infrastructure relied on the stability of permafrost but as permafrost thaws, the stability of the infrastructure is undermined, with critical consequences for many local businesses and the well being of the local inhabitants. Damage to infrastructure may also result in pollution.

The Russian Federation has recently published a national climate adaptation plan, designed to reduce Russia's vulnerability to the threat of climate change. Plans are to upgrade the national climate monitoring and forecasting systems, conduct assessments of the impacts of climate change and develop adaptation strategies. Actions include targeting changes in all design projects on the permafrost. These changes account for the melting processes and are applied to all newly developed establishments.

8 Conclusions

A large, rapid multi-method attribution study, supported by observational and large ensemble model analyses, indicates with high confidence that extremely warm periods such as the 6 months of January - June 2020 over the Siberian region would have been at least 2 °C cooler in a world without human influence. Similar events have a best estimate return time in the current climate of around 130 years and are now more than 600 times as likely to occur as they would have been at the beginning of the 20th century; with the best estimate orders of magnitude larger. By 2050 we expect such a regional warm period in the first 6 months of the year to be at least another 0.5 °C warmer, and possibly up to 5 °C warmer, with similar 6-month regional temperatures becoming correspondingly more frequent.

Statements regarding the very high June daily maximum temperatures (38 °C) such as were reported at Verkhoyansk can be made only with much lower confidence. Nevertheless, results also indicate a large increase in the likelihood of such temperatures and, with more confidence, an increase in extreme daily maxima of more than 1 °C when comparing the climate of 1900 to the present day.

References

[global-temperature-2020]
https://blog.metoffice.gov.uk/2020/06/23/global-temperature-how-does-2020-compare-so-far/

Ciavarella, A., Christidis, N., Andrews, M., Groenendijk, M., Rostron, J., Elkington, M., Burke, C., Lott, F. C., Stott, P. A. (2018). Upgrade of the HadGEM3-A based attribution system to high resolution and a new validation framework for probabilistic event attribution. Weather and Climate Extremes, Volume 20, https://doi.org/10.1016/j.wace.2018.03.003.

Choi, Y., and Ahn, J. (2019). Possible mechanisms for the coupling between late spring sea surface temperature anomalies over tropical Atlantic and East Asian summer monsoon. *Clim. Dyn.* 53, 6995–7009, https://doi.org/10.1007/s00382-019-04970-3.

Deser, C., Lehner, F., Rodgers, K.B. *et al.* (2020). Insights from Earth system model initial-condition large ensembles and future prospects. *Nat. Clim. Chang.*, 10, 277–286, https://doi.org/10.1038/s41558-020-0731-2.

Eyring, V., Bony, S., Meehl, G. A., Senior, C. A., Stevens, B., Stouffer, R. J., & Taylor, K. E. (2016). Overview of the Coupled Model Intercomparison Project Phase 6 (CMIP6) experimental design and organization. *Geoscientific Model Development*, *9*(5), 1937-1958.

Hansen, J., Ruedy, R., Sato, M., and Lo, K. (2010). Global surface temperature change, *Rev. Geophys.*, 48, RG4004, doi:10.1029/2010RG000345.

Harrington, L.J. and Friederike E. L. Otto, (2020). "Reconciling theory with the reality of African heatwaves", Nature Climate Change, https://doi.org/10.1038/s41558-020-0851-8.

Hazeleger, W., Wang, X., Severijns, C., Stefanescu, S., Bintanja, R., Sterl, A., Wyser, K., Semmler, T., Yang, S., Van den Hurk, B., et al. (2012). EC-Earth V2. 2: description and validation of a new seamless earth system prediction model, Climate dynamics, 39, 2611-2629.

Kovats, S. and Hajat, S. (2008). Heat Stress and Public Health: A Critical Review. Annual Review Public Health 29, 41-55 doi: 10.1146/annurev.publhealth.29.020907.090843.

Lehner, F., et al. (2020) "Partitioning climate projection uncertainty with multiple large ensembles and CMIP5/6." *Earth System Dynamics* 11.2: 491-508.

Maher, N., Milinski, S., Suarez-Gutierrez, L., Botzet, M., Dobrynin, M., Kornblueh, L., Kröger, J., Takano, Y., Ghosh, R., Hedemann, C., Li, C., Li, H., Manzini, E., Notz, N., Putrasahan, D., Boysen, L., Claussen, M., Ilyina, T., Olonscheck, D., Raddatz, T., Stevens, B. and Marotzke, J. (2019). The Max Planck Institute Grand Ensemble: Enabling the Exploration of Climate System Variability. Journal of Advances in Modeling Earth Systems, 11, 1-21. doi.org/10.1029/2019MS001639.

Mauritsen, T. et al. (2019). Developments in the MPI-M Earth System Model version 1.2 (MPI-ESM1.2) and Its Response to Increasing CO2, J. Adv. Model. Earth Syst.,11, 998-1038, doi:10.1029/2018MS001400.

McGregor, G. R., Bessemoulin, R., Ebi, K., & Menne, B. (Eds.). (2015). Heatwaves and health: Guidance on warning-system development (Vol. 1142). Geneva, Switzerland, World Meteorological Organization and World Health Organisation. Retrieved from: http://bit.ly/2NbDx4S.

Mueller, W.A. et al. (2018). A high-resolution version of the Max Planck Institute Earth System Model MPI-ESM1.2-HR. J. Adv. Model. EarthSyst.,10,1383–1413, doi:10.1029/2017MS001217.

O'Neill, B. C., Tebaldi, C., van Vuuren, D. P., Eyring, V., Friedlingstein, P., Hurtt, G., . . . Sanderson, B. M. (2016, sep). The scenario model intercomparison project (ScenarioMIP) for CMIP6. Geoscientific Model Development, 9 (9), 3461–3482. doi: 10.5194/gmd-9-3461-2016.

Taylor, Karl E., Ronald J. Stouffer, and Gerald A. Meehl (2012). An overview of CMIP5 and the experiment design. Bulletin of the American Meteorological Society 93.4, 485-498.

Wu, R., and S. Chen (2020). What Leads to Persisting Surface Air Temperature Anomalies from Winter to Following Spring over Mid- to High-Latitude Eurasia? J. Clim., 33, 5861–5883, https://doi.org/10.1175/jcli-d-19-0819.1.

Appendix

A1 Validation tables

Table A1: All models considered for analysis of Verkhoyansk station. For some models the number of ensemble members is indicated behind the model name in parentheses.

Model	Seasonal cycle	Spatial pattern	Sigma	Shape parameter	Conclusion
MPI-ESM1.2-HR	reasonable		3.388 (3.219 ... 3.543)	-0.298 (-0.358 ... -0.27)	bad, sigma too high
EC-Earth	good		3.012 (2.882 ... 3.131)	-0.277 (-0.305 ... -0.251)	bad, sigma too high
CMIP5-synthesis	NA	NA	2.78 (1.7 ... 4.67)	-0.28 (-0.38 ... -0.17)	reasonable
BCC_bcc-csm1-1-m	good	good	3.24 (3.02 ... 3.44)	-0.24 (-0.3 ... -0.19)	bad
CCCma_CanESM2	good	reasonable	2.81 (2.69 ... 2.94)	-0.26 (-0.3 ... -0.23)	bad
CMCC_CMCC-CESM	good	reasonable	3.13 (2.7 ... 3.47)	-0.38 (-0.45 ... -0.3)	bad
CMCC_CMCC-CMS	good	reasonable	2.81 (2.55 ... 3.05)	-0.3 (-0.42 ... -0.23)	reasonable
CNRM-CERFACS_CNRM-CM5	good	good	2.39 (2.29 ... 2.47)	-0.22 (-0.25 ... -0.2)	good
CSIRO-BOM_ACCESS1-0	good	good	2.52 (2.3 ... 2.71)	-0.24 (-0.3 ... -0.19)	good
CSIRO-BOM_ACCESS1-3	good	good	2.2 (2.01 ... 2.37)	-0.28 (-0.38 ... -0.22)	good
CSIRO-QCCCE_CSIRO-Mk3-6-0	good	reasonable	2.28 (2.21 ... 2.35)	-0.24 (-0.27 ... -0.22)	good
INM_inmcm4	good	reasonable	2.95 (2.65 ... 3.24)	-0.32 (-0.4 ... -0.25)	bad

IPSL_IPSL-CM5A-LR	good	good	1.85 (1.76 ... 1.94)	-0.26 (-0.29 ... -0.23)	reasonable
IPSL_IPSL-CM5A-MR	good	good	1.75 (1.62 ... 1.87)	-0.22 (-0.29 ... -0.17)	bad
IPSL_IPSL-CM5B-LR	good	good	1.98 (1.78 ... 2.17)	-0.31 (-0.41 ... -0.24)	good
MIROC_MIROC-ESM-CHEM	good	reasonable	4.5 (3.82 ... 5.05)	-0.39 (-0.52 ... -0.32)	bad
MIROC_MIROC-ESM	good	reasonable	4.58 (4.14 ... 4.99)	-0.41 (-0.55 ... -0.36)	bad
MIROC_MIROC5	good	reasonable	2.75 (2.63 ... 2.86)	-0.25 (-0.29 ... -0.22)	bad
MPI-M_MPI-ESM-LR	good	good	3.19 (3 ... 3.38)	-0.25 (-0.32 ... -0.21)	bad
MPI-M_MPI-ESM-MR	good	good	3.17 (2.95 ... 3.38)	-0.29 (-0.34 ... -0.25)	bad
MRI_MRI-CGCM3	good	good	2.64 (2.44 ... 2.82)	-0.23 (-0.28 ... -0.18)	reasonable
NASA-GISS_GISS-E2-H	good	good	2.21 (2.01 ... 2.39)	-0.2 (-0.33 ... -0.12)	good
NASA-GISS_GISS-E2-R	good	good	2.13 (1.93 ... 2.3)	-0.17 (-0.24 ... -0.1)	good
NCAR_CCSM4	good	good	3.71 (3.54 ... 3.9)	-0.32 (-0.38 ... -0.3)	bad
NCC_NorESM1-M	good	good	3.6 (3.42 ... 3.8)	-0.29 (-0.4 ... -0.26)	bad
NSF-DOE-NCAR_CESM1-BGC	good	good	3.49 (3.16 ... 3.81)	-0.32 (-0.46 ... -0.27)	bad
NSF-DOE-NCAR_CESM1-CAM5	good	reasonable	3.05 (2.8 ... 3.25)	-0.3 (-0.36 ... -0.25)	bad
HadGEM3-A	good	good	2.67 (2.55 ... 2.81)	-0.242 (-0.32 ... -0.22)	reasonable
ACCESS-CM2 (2)	good	good	2.52 (2.31 ... 2.78)	-0.3 (-0.37 ... -0.23)	good
ACCESS-ESM1-5 (3)	good	good	2.17 (2.01 ... 2.35)	-0.28 (-0.35 ... -0.21)	good
AWI-CM-1-1-MR (1)	good	good	3.52 (3.11 ... 4.04)	-0.28 (-0.38 ... -0.16)	reasonable (sigma too large)
BCC-CSM2-MR (1)	good	good	5.48 (4.84 ... 6.2)	-0.23 (-0.31 ... -0.13)	bad? (sigma way too large)
CMCC-CM2-SR5 (1)	good	good	2.5 (2.2 ... 2.87)	-0.23 (-0.34 ... -0.11)	good
CNRM-CM6-1 (1)	good	good	2.21 (1.95 ... 2.56)	-0.26 (-0.36 ... -0.14)	good
CNRM-CM6-1-HR (1)	good	good	2.34 (2.07 ... 2.69)	-0.25 (-0.35 ... -0.13)	good
CNRM-ESM2-1 (1)	good	good	2.07 (1.83 ... 2.39)	-0.15 (-0.25 ... -0.03)	good

CanESM5 (50)	good	good	2.87 (2.82 ... 2.92)	-0.32 (-0.33 ... -0.31)	reasonable (shape too small)
EC-Earth3 (3)	good	good	4.02 (3.76 ... 4.33)	-0.31 (-0.34 ... -0.28)	reasonable (sigma too large)
EC-Earth3-Veg (4)	good	good	3.81 (3.59 ... 4.08)	-0.33 (-0.37 ... -0.3)	bad (sigma too large; shape too small)
FGOALS-g3 (3)	good	good	2.98 (2.78 ... 3.23)	-0.29 (-0.33 ... -0.23)	good
GFDL-CM4 (1)	good	good	2.68 (2.35 ... 3.09)	-0.25 (-0.37 ... -0.11)	good
GFDL-ESM4 (1)	good	good	2.32 (2.05 ... 2.65)	-0.37 (-0.47 ... -0.25)	reasonable (shape too small)
HadGEM3-GC31-LL (4)	good	good	2.77 (2.59 ... 2.96)	-0.27 (-0.31 ... -0.22)	good
HadGEM3-GC31-MM (3)	good	good	2.58 (2.39 ... 2.79)	-0.09 (-0.12 ... -0.05)	good
INM-CM4-8 (1)	good	good	2.7 (2.39 ... 3.09)	-0.36 (-0.48 ... -0.24)	bad (sigma too large; shape too small)
INM-CM5-0 (1)	good	good	2.78 (2.49 ... 3.16)	-0.36 (-0.45 ... -0.26)	reasonable (shape too small)
IPSL-CM6A-LR (6)	good	good	2.9 (2.75 ... 3.07)	-0.25 (-0.3 ... -0.2)	good
KACE-1-0-G (2)	good	good	3.72 (3.39 ... 4.13)	-0.1 (-0.18 ... -0.01)	bad (somthing wrong with the data)
MIROC-ES2L (1)	good	good	2.41 (2.12 ... 2.74)	-0.25 (-0.34 ... -0.14)	good
MIROC6 (50)	good	good	2.46 (2.42 ... 2.51)	-0.3 (-0.31 ... -0.29)	good
MPI-ESM1-2-HR (2)	good	good	3.32 (3.03 ... 3.67)	-0.24 (-0.3 ... -0.15)	reasonable (sigma too large)
MPI-ESM1-2-LR (10)	good	good	3.27 (3.14 ... 3.42)	-0.31 (-0.34 ... -0.28)	reasonable (sigma too large)
MRI-ESM2-0 (2)	good	good	2.82 (2.57 ... 3.12)	-0.27 (-0.33 ... -0.19)	good
NESM3 (1)	good	good	2.92 (2.54 ... 3.36)	-0.18 (-0.32 ... -0.04)	good
NorESM2-MM (1)	good	good	3.05 (2.71 ... 3.49)	-0.34 (-0.44 ... -0.24)	bad (sigma too large; shape too small)
UKESM1-0-LL (5)	good	good	2.89 (2.74 ... 3.06)	-0.18 (-0.2 ... -0.16)	good

Table A2: All models considered for analysis of Siberian region. For some models the number of ensemble members is indicated behind the model name in parentheses.

Model / Observations	**Seasonal cycle**	**Spatial pattern**	**Sigma**	**Conclusion**
ERA5 (1979 - 2020)			1.036 (0.826 ... 1.197)	
GISS 250km anomalies			1.077 (0.917 ... 1.2)	

MPI-ESM1.2-HR (10)	good	good	1.094 (1.017 ... 1.167)	good
EC-Earth	good	reasonable	1.131 (1.074 ... 1.179)	reasonable Gaussian fit not good near event RP
CMIP5-synthesis	NA	NA	1 (0.73 ... 1.34)	good
BCC_bcc-csm1-1-m	good	good	0.96 (0.9 ... 1.02)	good
BNU_BNU-ESM	good	reasonable	0.99 (0.91 ... 1.07)	good
CCCma_CanESM2	good	reasonable	1.3 (1.25 ... 1.35)	bad
CMCC_CMCC-CESM	good	reasonable	1.02 (0.93 ... 1.11)	good
CMCC_CMCC-CMS	good	reasonable	1.03 (0.94 ... 1.11)	good
CNRM-CERFACS_CNRM-CM5	good	good	1.06 (1.03 ... 1.09)	good
CSIRO-BOM_ACCESS1-0	good	good	1.15 (1.09 ... 1.22)	good
CSIRO-BOM_ACCESS1-3	good	good	1.01 (0.95 ... 1.07)	good
CSIRO-QCCCE_CSIRO-Mk3-6-0	good	reasonable	0.69 (0.67 ... 0.71)	bad
FIO_FIO-ESM	good	reasonable	0.97 (0.92 ... 1.03)	good
INM_inmcm4	good	reasonable	1 (0.91 ... 1.08)	good
IPSL_IPSL-CM5A-LR	good	good	0.84 (0.81 ... 0.87)	good
IPSL_IPSL-CM5A-MR	good	good	0.83 (0.78 ... 0.87)	good
IPSL_IPSL-CM5B-LR	good	good	0.81 (0.75 ... 0.87)	reasonable
MIROC_MIROC-ESM-CHEM	good	reasonable	0.91 (0.83 ... 0.99)	good
MIROC_MIROC-ESM	good	reasonable	0.97 (0.9 ... 1.03)	good
MIROC_MIROC5	good	reasonable	0.94 (0.9 ... 0.97)	good
MPI-M_MPI-ESM-LR	good	good	1.1 (1.05 ... 1.15)	good, but excluded because MR-version gives same results
MPI-M_MPI-ESM-MR	good	good	1.08 (1.01 ... 1.14)	good
MRI_MRI-CGCM3	good	good	1.16 (1.09 ... 1.23)	good
NASA-GISS_GISS-E2-H-CC	good	good	0.9 (0.82 ... 0.96)	good

NASA-GISS_GISS-E2-H	good	good	0.85 (0.81 ... 0.88)	good
NASA-GISS_GISS-E2-R-CC	good	good	0.78 (0.7 ... 0.85)	reasonable
NASA-GISS_GISS-E2-R	good	good	0.85 (0.82 ... 0.89)	good
NCAR_CCSM4	good	good	1.14 (1.1 ... 1.17)	good
NCC_NorESM1-M	good	good	1.17 (1.1 ... 1.24)	good
NCC_NorESM1-ME	good	reasonable	1.3 (1.18 ... 1.4)	reasonable
NSF-DOE-NCAR_CESM1-BGC	good	good	1.19 (1.09 ... 1.28)	good
NSF-DOE-NCAR_CESM1-CAM5	good	reasonable	1.31 (1.24 ... 1.37)	bad
HadGEM3-A ALL	good	good	1.01 (0.96 ... 1.05)	good
ACCESS-CM2 (3)	good	good	1.33 (1.24 ... 1.43)	bad (sigma too high)
ACCESS-ESM1-5 (3)	good	good	1.44 (1.34 ... 1.56)	bad (sigma too high)
AWI-CM-1-1-MR (1)	good	good	1.11 (0.98 ... 1.27)	good
BCC-CSM2-MR (1)	good	good	1.02 (0.9 ... 1.16)	good
CAMS-CSM1-0 (2)	good	good	0.8 (0.73 ... 0.88)	reasonable (sigma too small)
CESM2 (5)	good	good	1.19 (1.12 ... 1.26)	good
CESM2-WACCM (3)	good	good	1.12 (1.04 ... 1.21)	good
CIESM (1)	good	good	1.2 (1.06 ... 1.36)	good
CMCC-CM2-SR5 (1)	good	good	1.02 (0.91 ... 1.16)	good
CNRM-CM6-1 (6)	good	good	1.26 (1.19 ... 1.32)	reasonable (sigma too large)
CNRM-CM6-1-HR (1)	good	good	0.99 (0.87 ... 1.13)	good
CNRM-ESM2-1 (5)	good	good	1.21 (1.15 ... 1.28)	reasonable (sigma too large)
CanESM5 (50)	good	good	1.19 (1.16 ... 1.21)	good
CanESM5-CanOE (3)	good	good	1.17 (1.09 ... 1.26)	good
EC-Earth3 (7)	good	reasonable	1.02 (0.98 ... 1.08)	good

EC-Earth3-Veg (4)	good	good	0.95 (0.9 ... 1.02)	good
FGOALS-f3-L (1)	good	good	1.18 (1.05 ... 1.35)	good
FGOALS-g3 (4)	good	good	1.07 (1.01 ... 1.15)	good
FIO-ESM-2-0 (3)	good	good	1.2 (1.12 ... 1.3)	good
GFDL-CM4 (1)	good	good	0.94 (0.83 ... 1.07)	good
GFDL-ESM4 (1)	good	good	0.81 (0.72 ... 0.93)	good
GISS-E2-1-G (1)	good	good	1.25 (1.1 ... 1.43)	reasonable (sigma too large)
HadGEM3-GC31-LL (4)	good	good	0.92 (0.86 ... 0.98)	good
HadGEM3-GC31-MM (3)	good	good	0.95 (0.89 ... 1.03)	good
INM-CM4-8 (1)	good	good	0.85 (0.75 ... 0.97)	good
INM-CM5-0 (1)	good	good	0.81 (0.71 ... 0.92)	reasonable (sigma too small)
IPSL-CM6A-LR (6)	good	good	1.05 (0.99 ... 1.1)	good
KACE-1-0-G (3)	good	good	1.41 (1.31 ... 1.51)	bad (something goes wrong with Tglob)
MCM-UA-1-0 (1)	good	reasonable	1.25 (1.1 ... 1.44)	reasonable (sigma too large)
MIROC-ES2L (1)	good	reasonable	0.81 (0.72 ... 0.93)	reasonable (sigma too small)
MIROC6 (50)	good	good	0.9 (0.88 ... 0.92)	good
MPI-ESM1-2-HR (2)	good	good	1.11 (1.01 ... 1.21)	good
MPI-ESM1-2-LR (10)	good	good	1.06 (1.02 ... 1.1)	good
MRI-ESM2-0 (2)	good	reasonable	1.28 (1.17 ... 1.4)	reasonable (sigma too large)
NESM3 (2)	good	good	1.33 (1.22 ... 1.46)	bad (sigma too high)
NorESM2-LM (1)	good	good	1.34 (1.18 ... 1.54)	reasonable (sigma too high)
NorESM2-MM (1)	good	good	1.17 (1.04 ... 1.34)	good
UKESM1-0-LL (5)	good	good	0.99 (0.94 ... 1.05)	good
MPI-GE (100)	good	good	1.08 (1.05 ... 1.1)	good

A2 Full synthesis figures

A2.1 Verkhoyansk station

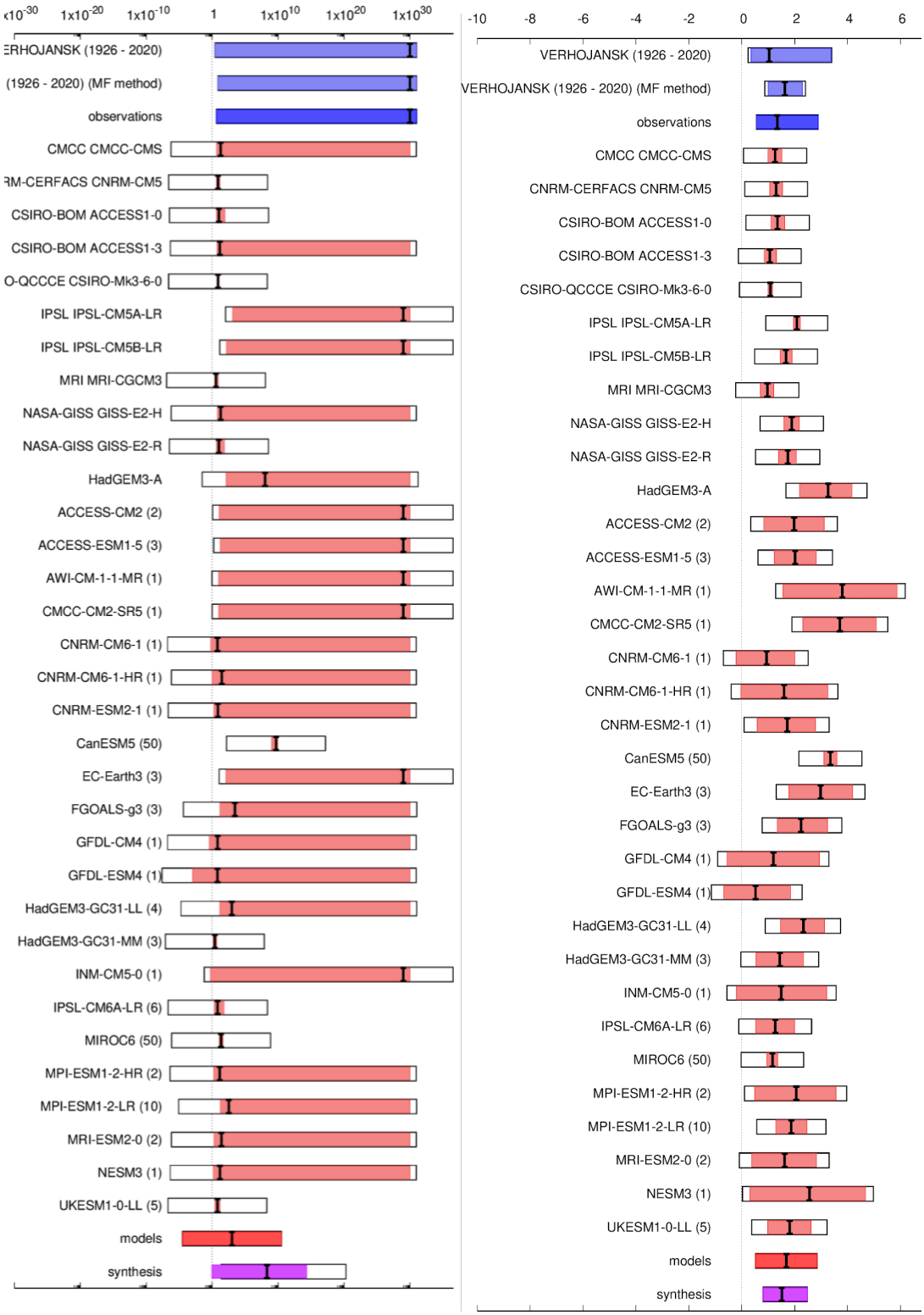

Figure A1: Synthesis of probability ratios (left) and changes in intensity (right) from the attribution analysis of June TXx at Verkhoyansk station.

A2.2 Siberian region

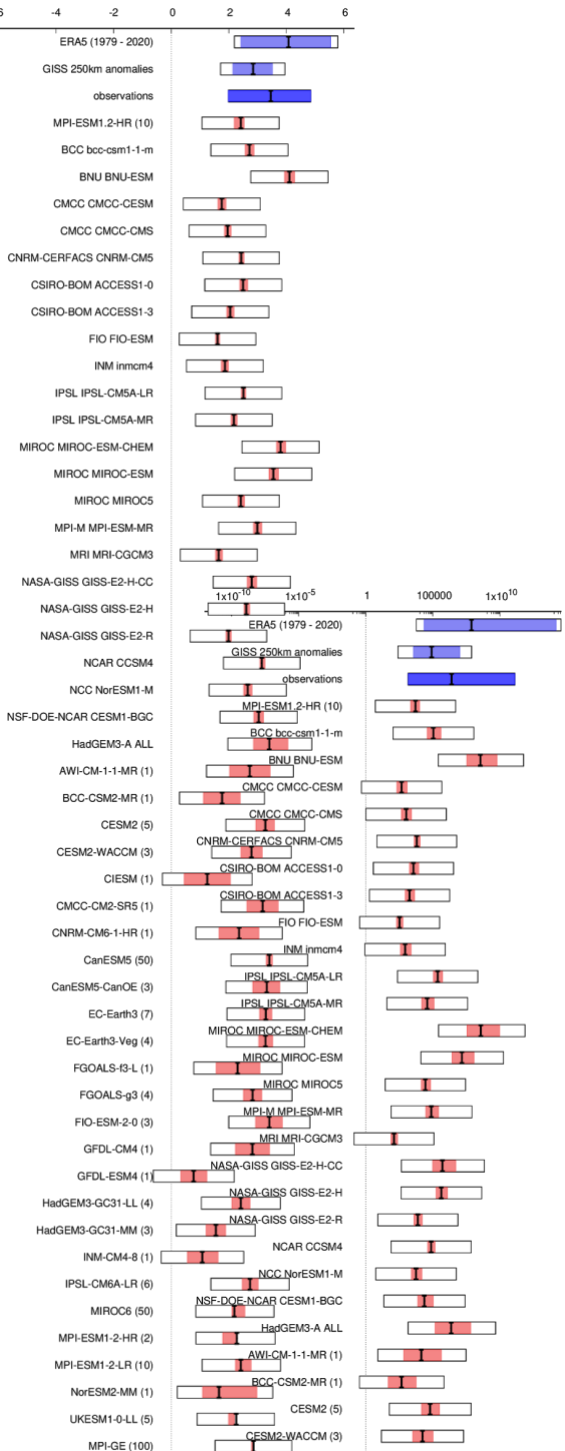
-6
-4
-2
0
2
4
6
ERA5 (1979 - 2020)
GISS 250km anomalies
observations
MPI-ESM1.2-HR (10)
BCC bcc-csm1-1-m
BNU BNU-ESM
CMCC CMCC-CESM
CMCC CMCC-CMS
CNRM-CERFACS CNRM-CM5
CSIRO-BOM ACCESS1-0
CSIRO-BOM ACCESS1-3
FIO FIO-ESM
INM inmcm4
IPSL IPSL-CM5A-LR
IPSL IPSL-CM5A-MR
MIROC MIROC-ESM-CHEM
MIROC MIROC-ESM
MIROC MIROC5
MPI-M MPI-ESM-MR
MRI MRI-CGCM3
NASA-GISS GISS-E2-H-CC
NASA-GISS GISS-E2-H
NASA-GISS GISS-E2-R
NCAR CCSM4
NCC NorESM1-M
NSF-DOE-NCAR CESM1-BGC
HadGEM3-A ALL
AWI-CM-1-1-MR (1)
BCC-CSM2-MR (1)
CESM2 (5)
CESM2-WACCM (3)
CIESM (1)
CMCC-CM2-SR5 (1)
CNRM-CM6-1-HR (1)
CanESM5 (50)
CanESM5-CanOE (3)
EC-Earth3 (7)
EC-Earth3-Veg (4)
FGOALS-f3-L (1)
FGOALS-g3 (4)
FIO-ESM-2-0 (3)
GFDL-CM4 (1)
GFDL-ESM4 (1)
HadGEM3-GC31-LL (4)
HadGEM3-GC31-MM (3)
INM-CM4-8 (1)
IPSL-CM6A-LR (6)
MIROC6 (50)
MPI-ESM1-2-HR (2)
MPI-ESM1-2-LR (10)
NorESM2-MM (1)
UKESM1-0-LL (5)
MPI-GE (100)
1x10-10
1x10-5
1
100000
1x1010
ERA5 (1979 - 2020)
GISS 250km anomalies
observations
MPI-ESM1.2-HR (10)
BCC bcc-csm1-1-m
BNU BNU-ESM
CMCC CMCC-CESM
CMCC CMCC-CMS
CNRM-CERFACS CNRM-CM5
CSIRO-BOM ACCESS1-0
CSIRO-BOM ACCESS1-3
FIO FIO-ESM
INM inmcm4
IPSL IPSL-CM5A-LR
IPSL IPSL-CM5A-MR
MIROC MIROC-ESM-CHEM
MIROC MIROC-ESM
MIROC MIROC5
MPI-M MPI-ESM-MR
MRI MRI-CGCM3
NASA-GISS GISS-E2-H-CC
NASA-GISS GISS-E2-H
NASA-GISS GISS-E2-R
NCAR CCSM4
NCC NorESM1-M
NSF-DOE-NCAR CESM1-BGC
HadGEM3-A ALL
AWI-CM-1-1-MR (1)
BCC-CSM2-MR (1)
CESM2 (5)
CESM2-WACCM (3)

Figure A2: Synthesis of probability ratios (left) and changes in intensity (right) from the attribution analysis of Jan-Jun mean temperature in Siberian region, comparing the 2020 event with 1900 climate.

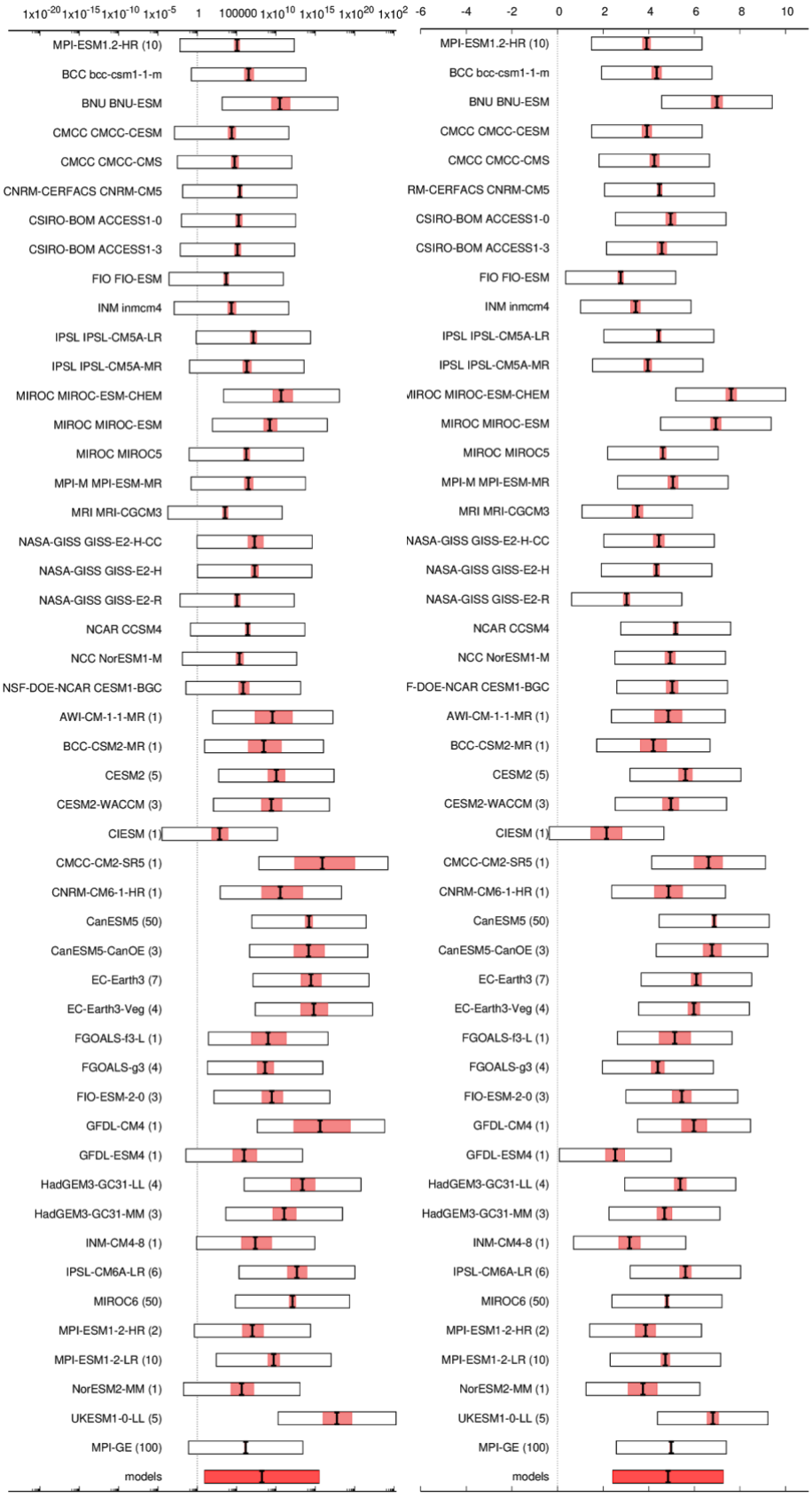

Figure A3: Synthesis of probability ratios (left) and changes in intensity (right) from the attribution analysis of Jan-Jun mean temperature in Siberian region, comparing future 2050 climate with 1900 climate.